The Astrophysical Journal, 634:287–313, 2005 November 20

ON THE ACCRETION ORIGIN OF A VAST EXTENDED STELLAR DISK AROUND THE ANDROMEDA GALAXY

R. Ibata,[1] S. Chapman,[2] A. M. N. Ferguson,[3] G. Lewis,[4] M. Irwin,[5] and N. Tanvir[6]

Received 2005 April 6; accepted 2005 July 13

ABSTRACT

We present the discovery of an inhomogenous, low surface brightness, extended disklike structure around the Andromeda galaxy (M31) based on a large kinematic survey of more than 2800 stars with the Keck DEIMOS multiobject spectrograph. The stellar structure spans radii from 15 kpc out to ~40 kpc, with detections out to $R \sim 70$ kpc. The constituent stars have velocities close to the expected velocity of circular orbits in the plane of the M31 disk and typically have a velocity dispersion of ~30 km s^{-1}. The color range on the upper red giant branch shows a large spread indicative of a population with a significant range of metallicity. The mean metallicity of the population, measured from Ca II equivalent widths, is [Fe/H] $= -0.9 \pm 0.2$. The morphology of the structure is irregular at large radii and shows a wealth of substructures that must be transitory in nature and are almost certainly tidal debris. The presence of these substructures indicates that the global entity was formed by accretion. This extended disk follows smoothly on from the central parts of M31 disk out to ~40 kpc with an exponential density law with a scale length of 5.1 ± 0.1 kpc, which is similar to that of the bright inner disk. However, the population possesses similar kinematic and abundance properties over the entire region where it is detected in the survey. We estimate that the structure accounts for approximately 10% of the total luminosity of the M31 disk, and given the huge scale, contains ~30% of the total disk angular momentum. This finding indicates that at least some galactic stellar disks are vastly larger than previously thought and are formed, at least in their outer regions, primarily by accretion.

Subject headings: galaxies: evolution — galaxies: individual (M31) — galaxies: structure — Local Group

Online material: color figures

1. INTRODUCTION

Within the framework of hierarchical structure formation, large spiral galaxies like the Milky Way or Andromeda (M31) arose from the merger of many small galaxies and protogalaxies that began coalescing at high redshift. During this process, considerable dynamical and chemical evolution took place, as the primordial galaxy fragments were assimilated, stellar populations evolved and fed enriched gas back into the interstellar medium, and fresh gas was accreted onto the galaxy. The disk, the defining component of spiral galaxies, formed through dissipative processes, growing from the inside out mainly by the accretion of gas with high angular momentum with probably only a small component of accreted stars (Abadi et al. 2003).

The structure of disks is generally exponential in both their radial and vertical directions. A striking feature of this component of galaxies is the tendency for it to be truncated radially at 3–4 scale lengths (van der Kruit & Searle 1981; Pohlen et al. 2000). This distance would correspond to ~12 kpc in the Milky Way and ~20 kpc in M31. Although we still lack a solid understanding of how and why these truncations occur, evidence suggests an abrupt change in the star formation efficiency across this boundary, perhaps related to a shift in the dominant star formation mode (Kennicutt 1989; Ferguson et al. 1998; Schaye 2004). The fact that disk stars are detected beyond the predicted truncation radii in the Milky Way and M31, as well as in several lower mass galaxies (e.g., NGC 300 [Bland-Hawthorn et al. 2005]; M33 [A. Ferguson et al. 2005, in preparation]), is intriguing. Did these stars form in situ? If so, did they form a long time ago during the very early stages of disk evolution, or have they formed much more recently from newly acquired gas? On the other hand, could they have been tidally stripped from infalling satellites on close to coplanar orbits?

In order to address these questions and examine galaxy formation models in detail, our group has undertaken a deep panoramic study of the Andromeda galaxy, which, when set in contrast with the Milky Way, was to serve as a test case against which formation simulations could be compared. Studies of the Milky Way are naturally blessed with more photons than those of more distant systems, and by resolving individual stars and measuring their kinematic and chemical properties one can study the formation of our Galaxy in a detail and with a mass and spatial resolution that can only be dreamed of elsewhere. However, thanks to advances in instrumentation, it is now also possible to measure the kinematics and chemistry of individual stars in galaxies of the Local Group. One of the major benefits that this affords us is a global view of a galaxy, freeing us from much of the projection uncertainties that our position within the Milky Way plagues us with, and yet retaining the fine detail that spectroscopic studies of resolved stellar populations provide.

Located at a distance of 785 ± 25 kpc [$(m - M)_0 = 24.47 \pm 0.07$; McConnachie et al. 2005], Andromeda is the closest giant spiral galaxy to our own, and the only other giant galaxy in the Local Group. As such, it is often considered to be the "sister" galaxy to the Milky Way. Recent studies suggest that the two galaxies do indeed have very similar total masses (including the dark matter; Evans et al. 2000; Ibata et al. 2004), yet there are significant differences between them. M31 is slightly more luminous than the Milky Way, and it has a higher rotation curve and a bulge

[1] Observatoire de Strasbourg, 11, rue de l'Université, Strasbourg F-67000, France.
[2] California Institute of Technology, Pasadena, CA 91125.
[3] Institute for Astronomy, University of Edinburgh, Royal Observatory, Blackford Hill, Edinburgh EH9 3HJ, UK.
[4] Institute of Astronomy, School of Physics, A29, University of Sydney, NSW 2006, Australia.
[5] Institute of Astronomy, Madingley Road, Cambridge CB3 0HA, UK.
[6] Physical Sciences, University of Hertfordshire, Hatfield AL10 9AB, UK.

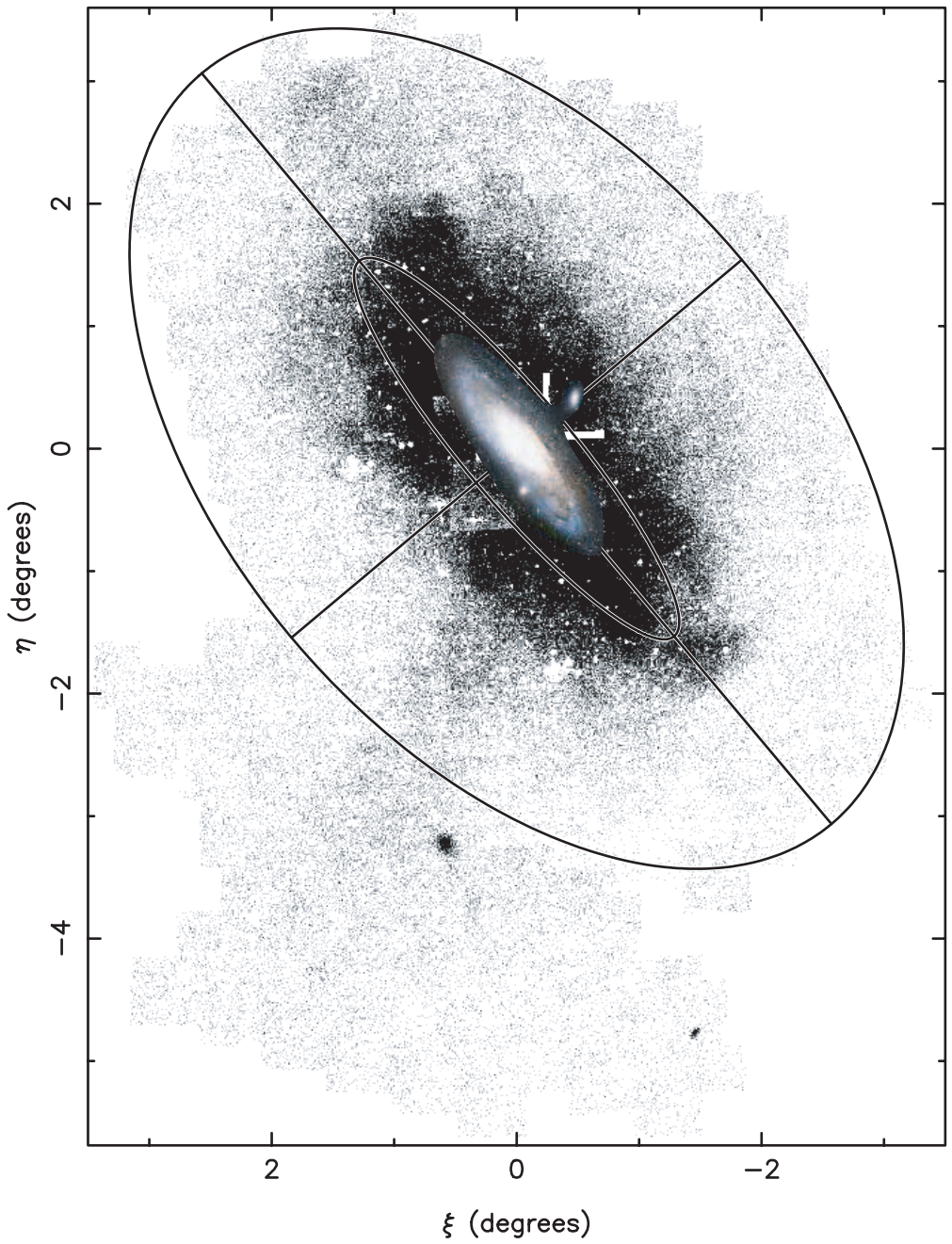

FIG. 1.—Current coverage of our large panoramic survey of M31 with the INT camera, in standard coordinates (ξ, η). The outer ellipse shows a segment of a 55 kpc radius ellipse flattened to $c/a = 0.6$, and the major and minor axis are indicated with straight lines out to this ellipse. A Digitized Sky Survey image of the central galaxy has been inserted to scale. The map shows the distribution of RGB stars throughout the halo. The most striking structure in the map is a vast flattened inner structure, of major axis extent $\sim 4^\circ$, a messy inhomogenous entity that envelops the familiar bulge and disk of M31.

with higher velocity dispersion. M31 possesses a globular cluster system with $\sim$500 members, approximately 3 times more numerous than that of the Milky Way, and contains several members of a type of luminous extended cluster not present around the Galaxy (Huxor et al. 2005). The disk of Andromeda is also much more extensive, with a scale length of 5.9 ± 0.3 kpc (R-band value corrected for a distance of 780 kpc; Walterbos & Kennicutt 1988) compared to 2.3 ± 0.1 for the Milky Way (Ruphy et al. 1996), but which is currently forming stars at a lower rate than the Galaxy (Avila-Reese et al. 2002; Walterbos & Braun 1994). Although possibly the consequence of low-number statistics, it is tempting to attribute significance to the fact that Andromeda has four dwarf elliptical galaxies (M32, NGC 205, NGC 147, and NGC 185) among its entourage of satellites and no star-forming dwarf irregulars, whereas the Milky Way has none of the former but two of the latter. However, it is perhaps in their halo populations that the differences between the two galaxies are most curious and most interesting. It has been known for many years that M31 does not possess the "textbook" stellar halo model developed from observations of the Milky Way. Minor axis halo fields have shown startlingly high metallicities ($[\mathrm{Fe/H}] \sim -0.5$) and an $R^{1/4}$-law density profile (Durrell et al. 2004), unlike the $R^{-3.5}$ behavior of the metal-poor Galactic halo (Chiba & Beers 2000). Nevertheless, recent studies of M31 confirm that an old, metal-poor halo lurks

beneath (Holland et al. 1996; Durrell et al. 2001; Reitzel & Guhathakurta 2002; Brown et al. 2003). Both the de Vaucouleurs profile and the high metallicity are suggestive of an active merger history at the time of halo (or bulge) formation.

The photometric data set that forms the foundation of this study was obtained with the Wide Field Camera at the 2.5 m Isaac Newton Telescope (INT); the survey and preliminary results were presented in Ibata et al. (2001a) and Ferguson et al. (2002), although the full completed survey will be discussed in detail in a forthcoming article (M. Irwin et al. 2005, in preparation). The density of red giant branch (RGB) stars throughout the survey region, which now covers $\sim$40 deg^2, is reproduced in Figure 1, onto which we have superimposed the familiar Digitized Sky Survey image constructed from Palomar plates. The solid angle covered by the INT survey corresponds to a projected area of $\sim$7400 kpc^2 at the distance of M31. As shown in the earlier publications in this series, the INT survey revealed a wealth of substructure throughout the "halo" of M31. However, the most prominent of the details that we uncovered was the presence of a gigantic extended flattened structure, seen clearly in Figure 1 as a dense component that surrounds M31 with approximately elliptical global shape but with significant small-scale irregularities, spanning up to $\sim$40 kpc from the galaxy center, almost twice the maximum extent of the bright inner disk. Due to the expectations from galaxy formation simulations with cold dark matter, our initial interpretation of this structure favored the possibility that it was a flattened inner halo (Katz & Gunn 1991; Summers 1993; Steinmetz & Müller 1995) with significant spatial substructure (Klypin et al. 1999; Moore et al. 1999). However, the proximity of M31 has allowed us to follow up these detections with deep Keck DEIMOS spectroscopic observations (initial results of the spectroscopic survey were presented in Ibata et al. 2004). It is the radial velocities and metallicities derived from these deep spectroscopic data that we present and analyze in this contribution.

The layout of this paper is as follows. In § 2 we first discuss the global geometry of M31 and the inclination angle of the disk, and fit an exponential function to the major axis photometry. The spectroscopic observations are presented in § 3, and the resulting kinematics in § 4. In § 5 we examine several fields in more detail, also presenting their mean metallicity and fitting global trends. These data are interpreted in § 6, where we present several possibilities for the formation of the structure, and we finish in § 7 with the conclusions of the study.

2. SIMPLE GLOBAL STRUCTURAL MODEL OF M31

Before describing the observations and analysis of the kinematic data set, it is useful to discuss the large-scale structure of M31. Andromeda is observed highly inclined to the line of sight with $i = 77^\circ$ (Walterbos & Kennicutt 1988), and it is seen on the sky with a position angle of 38° east of north (Walterbos & Kennicutt 1987). Within an angular distance of 90′ (20.4 kpc), Walterbos & Kennicutt (1988) find a good fit with the sum of a bulge model together with a disk model of *R*-band scale length 5.9 ± 0.3 kpc (corrected for a distance of 780 kpc).

To compare these findings to our INT survey, we measure the source density in a color-magnitude box designed to select the brightest RGB stars 1.5 mag below the RGB tip. Sources with *I*-band magnitudes in the range $20.0 < i_0 < 21.5$ and colors $1.0 < (V - i)_0 < 4.0$ are selected. (The Schlegel et al. [1998] dust maps are used throughout this work to correct the INT photometry for extinction.) We correct the star counts for crowding using the approach of Irwin & Trimble (1984), and subtract a small background count as determined from fields at the edge of the survey.

The deprojected positions of the RGB stars are binned in a polar coordinate grid with 5° azimuthal bins and 0.5 kpc radial bins. The azimuthal counts at a given radius are then medianed together in groups of 5 (i.e., covering 25°), and we step around the circle in intervals of 15°. The top panel of Figure 2 shows the four profiles within a deprojected angle of ±35° of the major axis (i.e., ±7.°9 projected), assuming an inclination of $i = 77^\circ$, with the additional thick-lined profile showing the median of all 14 bins of 5° width. Positive radius means that the medianed area is on the northeastern major axis, and negative radius means that it is on the southwestern major axis. The abscissa *R* is a deprojected radius that assumes the stated inclination. The artificial drop in the source counts inside of $R \sim 18$ kpc is due to crowding.

Evidently the major axis profile is close to exponential; it is fitted in the bottom panel with a model (*dashed line*) of scale length 5.1 ± 0.1 kpc. This scale length is similar to that of the inner disk, so it appears that the large-scale properties of the outer disk structure follow on smoothly from those of the inner disk. The uncertainties in the median profile derived purely from the Poisson statistics of the star counts are also shown in the bottom panel of Figure 2. These Poisson errors are quite small compared to the variations between the profiles in the different azimuthal slices shown in the top panel, indicating that the differences reflect the presence of real nonaxisymmetric structures in the disk, which include spiral arms as well as possible tidal debris.

The top panel of Figure 3 shows the profiles for all azimuthal bins. The large discrepancies between the different profiles are very obvious, with the less steep profiles corresponding to azimuthal bins toward the minor axis. The higher number densities on the minor axis are largely due to the huge bulge component in M31. Indeed, in the bulge-disk decomposition of Walterbos & Kennicutt (1988), the bulge dominates over the disk at all radii on the minor axis. However, part of this variation may also come from a change in the inclination of the galaxy at large radius. To explore this possibility, we fitted the value of *i* by assuming that the most likely inclination is that having the lowest rms dispersion about the median profile in the distance interval 20 kpc $< R <$ 40 kpc. The corresponding profiles are shown in the bottom panel of Figure 3, together with the medianed profile (*thick black line*). The fitted inclination angle is $i = 64.^\circ7$.

With this smaller inclination, the surface density profiles are now much more similar, yet there are still variations between the profiles of up to a factor of $\sim$2–3 at a given radius, due in part to the presence of obvious "lumps." Fitting the median profile in the range 20 kpc $< R' <$ 40 kpc with an exponential law yields a scale length of 7.8 ± 0.07 kpc. This larger scale-length value compared to the previous major axis exponential fit demonstrates a failure in our simple tilted disk model. A more complex model with a bulge component is required to fit the central regions of the galaxy more reliably, yet this cannot be constructed from our INT star-count data which are highly incomplete inside of $R \sim 15$ kpc.

It is noteworthy that analyses of the kinematics of H I gas (e.g., Brinks & Burton 1984 and references therein) show that the outer regions of the gaseous disk are more highly inclined with respect to the line of sight, appearing almost edge-on. This behavior is opposite to what we tentatively infer here from the distribution of stars. However, since the outer gas disk can respond to pressure, and may be much younger than the stars at that location, the gas and the stellar disks need not accurately trace each other.

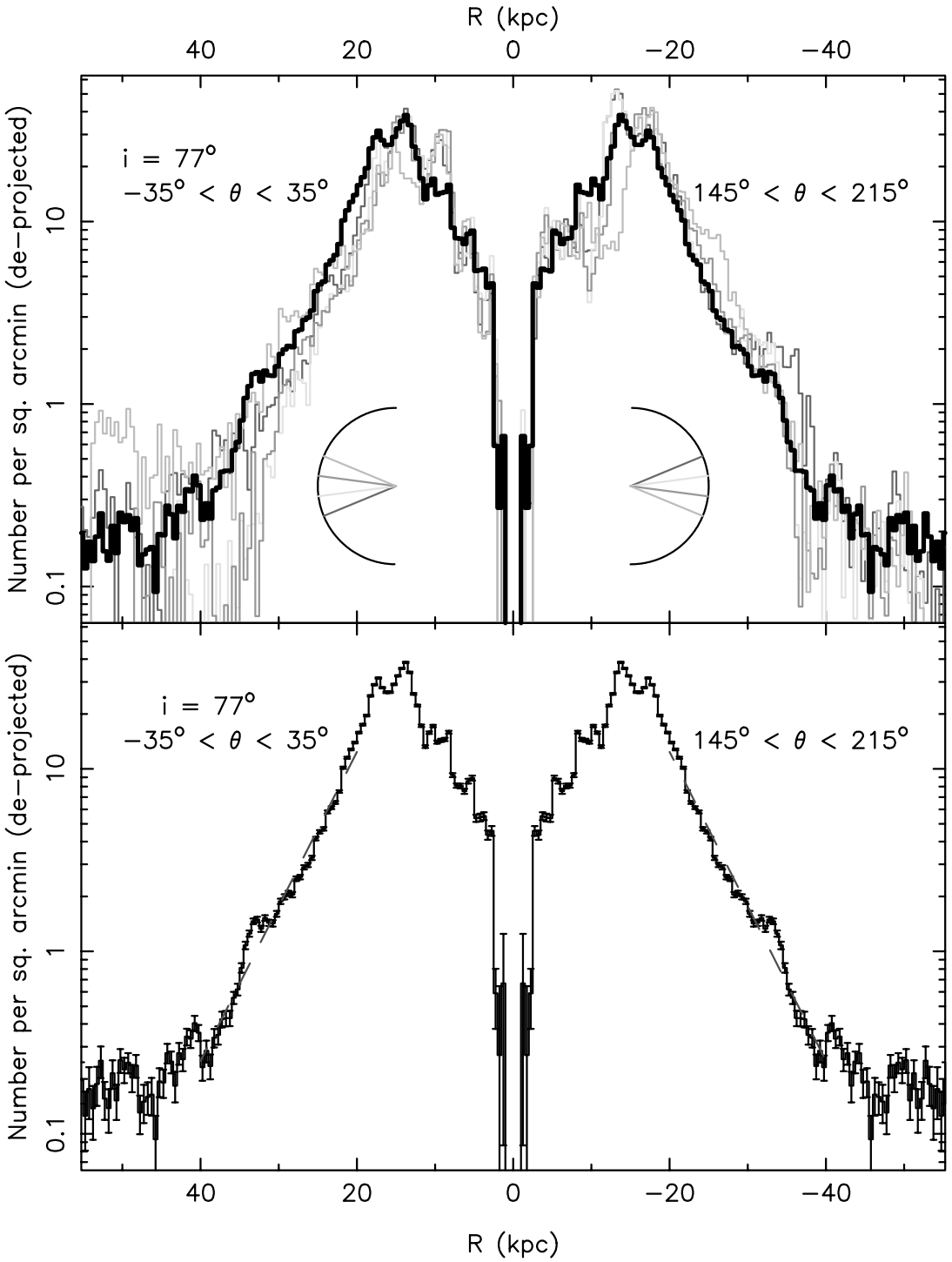

FIG. 2.—*Top:* Density profiles close to the major axis. Positive abscissa values correspond to deprojected radii toward the northeastern side of M31. The thin lines are the density profiles medianed over 5° deprojected azimuthal bins, assuming a galaxy inclination of $i = 77°$. The four profiles to the northeast cover the deprojected angles $-35° < \theta < -10°$, $-20° < \theta < 5°$, $-5° < \theta < 20°$, and $10° < \theta < 35°$, with the four profiles to the southwest being identical cuts rotated by 180°. The small semicircle inserted into this diagram represents the two (deprojected) halves of the galaxy, with the radial lines indicating the central angle of the wedges, with the same color scheme as the density profiles. The thick black line corresponds to the median of all 14 azimuthal bins in the range $-35° < \theta < 35°$. *Bottom:* An exponential fit to the medianed profile in the range 20 kpc $< R <$ 40 kpc, with a scale length 5.1 $\pm$ 0.1 kpc. The Poisson uncertainties in the medianed profile are also displayed. [*See the electronic edition of the Journal for a color version of this figure.*]

In the following discussion, we present results based on inclination values of $i = 77°$ and $i = 64.°7$; this will help clarify the uncertainty due to a possible tilt of the outer disk with respect to the inner disk. Deprojected quantities, such as the deprojected radius R or the velocity lag $v_{\rm lag}$ (defined below) will implicitly assume an inclination of $i = 77°$; primed versions of these variables (e.g., R', $v'_{\rm lag}$) will instead correspond to the lower inclination case of $i = 64.°7$.

3. OBSERVATIONS

During eight Keck nights (~75% useful time) in 2002 September, 2003 September, and 2004 September, we undertook

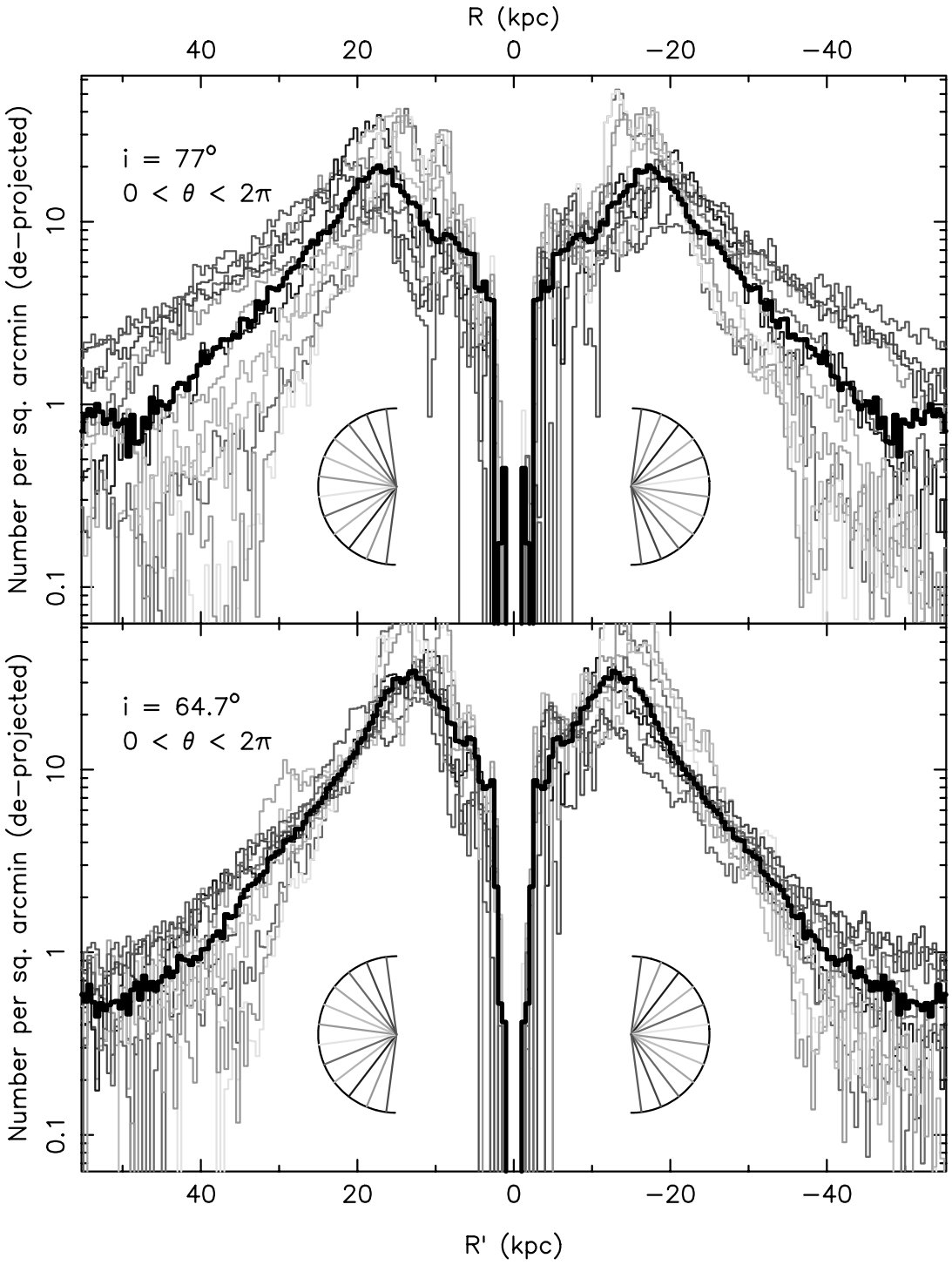

FIG. 3.—*Top:* Medianed density profiles at different position angles around M31, offset at 15° from each other, assuming a galaxy inclination of $i = 77°$. As in Fig. 2, each profile is constructed from a median of five consecutive azimuthal bins of width 5°, and the semicircular insert explains the color code. The thick black line corresponds to the median of all azimuthal bins. *Bottom:* Similar profiles, but for an inclination angle of $i = 64.°7$, fitted to minimize the dispersion around the median profile of all azimuthal bins over the interval 20 kpc $< R' <$ 40 kpc. [*See the electronic edition of the Journal for a color version of this figure*.]

a DEIMOS program to spectroscopically follow up the detected substructures in M31 to measure their kinematics and to begin a complete kinematic portrait of M31 systematically targeting disk and halo fields. The observing runs have employed the standard high-resolution DEEP2 slit-mask approach (e.g., Davis et al. 2003) covering the wavelength range 6400–9000 Å, with a spectral resolution of ~0.6 Å. The observations have also pioneered two new approaches with DEIMOS: a band-limiting ~300 Å Ca II triplet filter to multiplex ~4″ slitlets in the spectral direction yielding as many as 800 slits per mask, and a "fiber hole" 0.″7 slitlet approach packing ~600 holes per mask. This fiber-hole approach, adopted in 2004 September, proved to be very successful, giving Poisson-limited sky subtraction (down to $i = 21.5$) by assigning holes to monitor the sky spectrum; longer slitlets simply waste valuable CCD real estate in regions of high target density. The fiber-hole diameters were milled at 0.″7 to match the median seeing. The data set presented in this paper is the sum of all the "standard mask" spectra plus "fiber-hole"

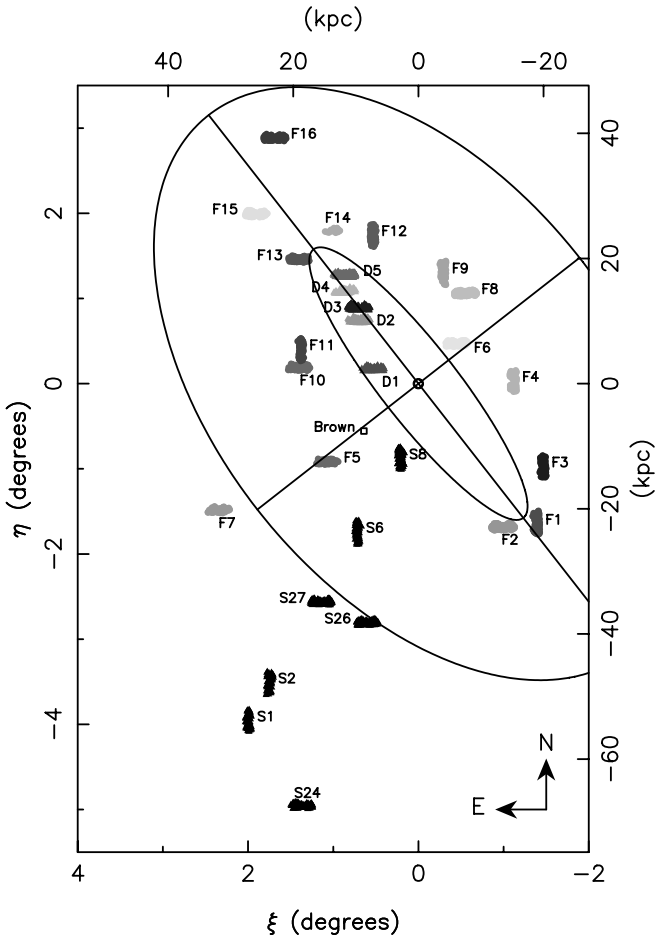

FIG. 4.—Distribution of Keck DEIMOS fields in relation to the survey region depicted in Fig. 1. For clarity, we have divided these fields into three groups. The fields in the giant stream (*black*) are prefixed by the letter S, and we keep the same field names as in Ibata et al. (2004), with the addition of fields S24, S26, and S27. Those fields located within the inner ellipse are denoted D1–D5. The remaining fields are named F1–F16. The color coding adopted here for fields D1–D5 and F1–F16 helps identify the locations of the data presented later in Figs. 9, 11, 12, and 14. The small square labeled "Brown" on the southeastern minor axis marks the location of the deep photometric study of Brown et al. (2003), whose relevance to the present work we discuss in § 6. [*See the electronic edition of the Journal for a color version of this figure.*]

spectra obtained up to 2004 September that do not use the band-limiting filter. A total of 28 fields were observed in this way. The layout of these spectroscopic fields is displayed in Figure 4: the five fields D1–D5 probe the M31 disk, the 16 fields F1–F16 probe both the halo and what we considered to be "halo" over-densities, while seven fields were assigned to investigate the dynamics of the giant stream (Ibata et al. 2001a), which is seen clearly in Figure 1 as an elongated structure to the southeast of M31.

For each of these fields except the stream fields, the highest priority targets were selected for observation from the INT survey within a color-magnitude box with *I*-band magnitudes in the range $20.5 < i < 22.0$ (without reddening correction) and colors $1.0 < (V - i)_0 < 4.0$. This broad selection was designed to pick out a wide range of RGB stars, containing both metal-poor and metal-rich populations (further details will be provided in M. Irwin et al. 2005, in preparation). Other nonsaturated targets brighter than $i = 22$ were also chosen by an automated selection algorithm at lower priority to fill in available space on the spectrograph detector.

Each mask was observed for typically three integrations of 20 minutes each. The spectroscopic images were processed and combined using the pipeline software developed by our group. This software debiases, performs a flat field, extracts, wavelength-calibrates, and sky-subtracts the spectra. The radial velocities were measured by cross-correlating against a model template with Gaussian functions at the rest-frame wavelength positions of the Ca II triplet lines (the technique used is similar to that discussed by Wilkinson et al. 2004). An estimate of the radial velocity uncertainty is then obtained for each star from the dispersion of the radial velocity measured from the three Ca II triplet lines separately. The accuracy of these data are very good for such faint stars, with typical uncertainties of 5–10 km s^{-1}. The sample presented in this paper consists of 2834 stars with velocity uncertainties <20 km s^{-1} that fall into the above RGB color-magnitude selection window.

4. RESULTS

The velocity distribution of all the targeted stars with $(V - i)_0 > 1.0$ is displayed in the top panel of Figure 5. This distribution is a mixture of bona fide M31 stars plus a contamination from Galactic stars. We have superimposed the expected Galactic contribution over a 240 arcmin^2 area in the direction of M31 according to the Besançon Galactic star-count model (Robin et al. 2004), onto which we have applied the color-magnitude selection window used for spectroscopic target selection. Since we have not observed every star in each field, and since the ratio of M31 to Milky Way stars varies dramatically from the inner fields to the outer fields, we cannot easily scale the model predictions. For the illustrative purposes of Figure 5, we have chosen a normalization to match the Besançon model to our observed distribution for velocities higher than the peak in the model. We will return to the issue of Galactic contamination in our analysis of field F16 (Fig. 24), placing an upper limit on the model normalization, which shows that Galactic contamination is low at heliocentric radial velocities below -100 km s^{-1}. It is clear from a visual comparison of the distributions in Figure 5 that we observe a large number of stars in significant excess over the expected distribution of contaminants. The apparent mismatch between the peak in the observed distribution and the Besançon model is due to the large number of stars observed in disk fields D1–D5 on the northeastern side of Andromeda, which combine in this summed-up plot to give a broader peak centered on -60 km s^{-1}. If we instead sum up the 11 fields on the southern side of the minor axis (fields F1–F4 and all the stream fields), the rotation of the M31 disk separates Galactic stars from the majority of stars in Andromeda, allowing a cleaner discrimination. This is shown in the bottom panel of Figure 5. These considerations show that by selecting stars with velocities <-100 km s^{-1} we can drastically minimize the Galactic contamination, incurring only the penalty of including a small fraction of Galactic halo stars into our sample; furthermore, these remaining Galactic halo stars are expected to have a relatively flat distribution in radial velocity.

Due to the wide coverage of the spectroscopic fields, it is useful to compare the observed velocity of a star with the expected radial velocity of a population moving in circular orbits. To this end, we construct a simple model assuming a slight variant on the geometrical model of Brinks & Burton (1984), which was fitted to the distribution of flux and kinematics of H I gas in M31. The Brinks & Burton (1984) model comprises a disk of exponential thickness 0.12 kpc out to 16 kpc, at which radius the disk starts to flare, with a thickness that increases linearly with radius up to a value of 1.686 kpc at a radius of 30.5 kpc. This model for the H I gas is too thin to provide a reasonable representation of the inner stellar disk, however. We adopt instead a more realistic disk scale height value of 0.35 kpc, as derived for

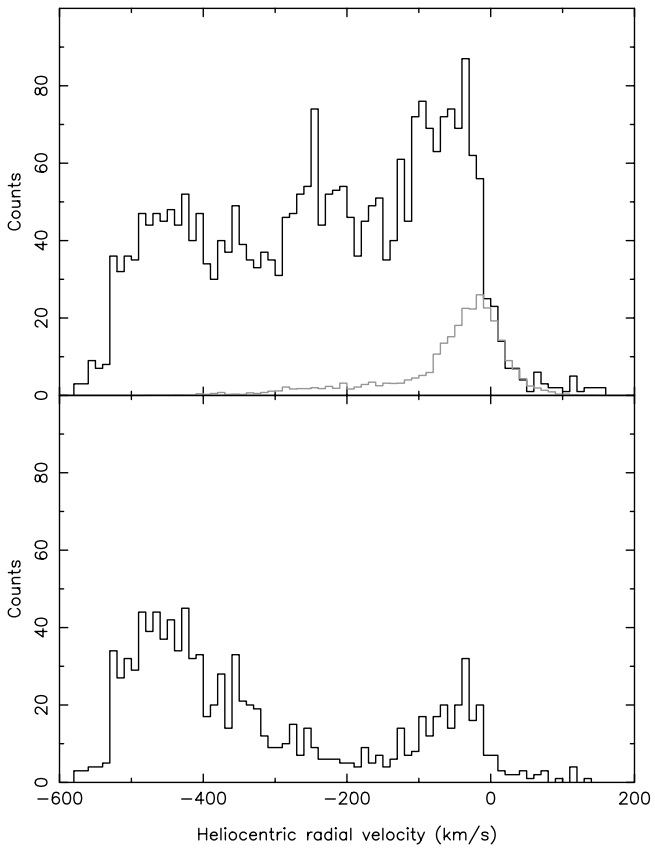

FIG. 5.—*Top:* Velocity distribution of the 2834 RGB star candidates in all fields shown in Fig. 4 that pass our color-magnitude and spectrum quality criteria. The light-gray histogram shows the prediction of the Besançon Galactic model for an area of 240 arcmin^2 within our color-magnitude selection window. With this normalization, the model fits the high-velocity edge of the observed velocity distribution. *Bottom:* The summed distribution of stars in the fields F1–F4 plus all the stream fields. [*See the electronic edition of the Journal for a color version of this figure.*]

the old disk of the Milky Way (Gilmore & Reid 1983). This scale height is taken to be constant within 16 kpc, beyond which we assume that the stellar disk begins to flare with a scale height that increases linearly with radius, attaining a maximum scale height of 1.686 kpc at a radius of 30.5 kpc. Beyond that radius we assume that the disk has constant thickness. Contrary to the Brinks & Burton (1984) H I model, we do not introduce a warp into the plane of the stellar disk. We assume that the disk is exponential both in the vertical and radial directions, with a radial scale length of 5.1 kpc, as deduced in § 2 above.

We integrate along the line of sight through this flaring exponential disk model and project onto the line of sight the kinematics of circular orbits. For this, we adopt the circular velocity curve compilation of Klypin et al. (2002), which joins CO measurements from Loinard et al. (1995) for $R < 10$ kpc with H I measurements by Brinks & Burton (1984) at larger radii; these data are reproduced in Figure 6, along with our spline fit, which is shown adjusted for the small inclination correction. The dip in the rotation curve near 5 kpc is, of course, an artifact of noncircular motions in the gas at that location, and is unimportant for the present work since our fields all lie beyond that radius.

The resulting map of the average projected rotation velocity over the inner region of our survey is shown with gray contour lines in Figure 7. Since the scale height of the stellar disk model that forms the basis of this map is highly uncertain, we also show in Figure 7 the effect of doubling the scale height of the model

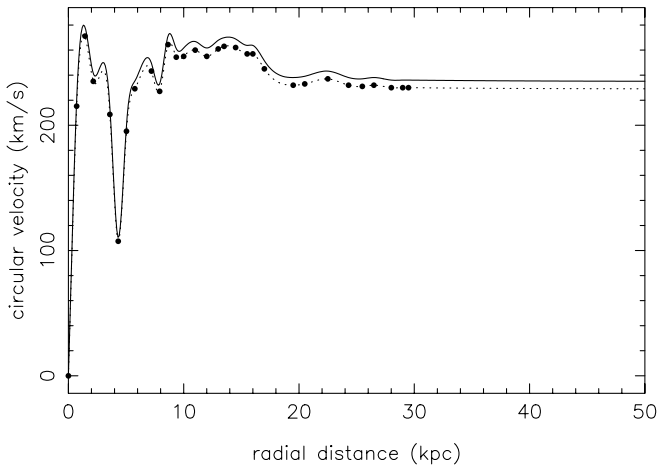

FIG. 6.—Rotation curve of M31. The points show a rotation curve compilation by Klypin et al. (2002), which is derived from CO rotation velocities measurements (Loinard et al. 1995) for $R < 10$ kpc, and from the rotation velocity of the H I (Brinks & Burton 1984) beyond that radius. The dotted line shows a spline fit to these data, while the continuous line indicates the correction for the 77° inclination of the inner disk of this galaxy.

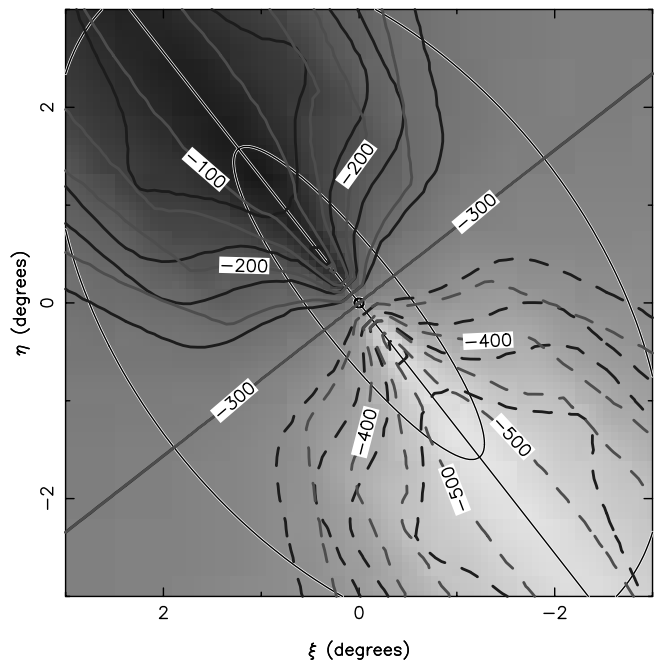

FIG. 7.—Gray-scale image and gray contour lines show a simple model for the expected velocity of stars on circular orbits as a function of position around M31, made by projecting the flaring exponential disk model discussed in the text. Matter in this model has a velocity that is tangential to the cylindrical coordinate R in the plane of M31, with a speed interpolated from the curve of Fig. 6. The thickness of the disk model (which has a maximum scale height of 1.686 kpc), coupled with the high inclination, means that a given line of sight intersects matter over a significant range in galactic radius, where the circular velocity, and its projection onto the line of sight, can be different. Hence this map shows the *average* expected velocity for stars on circular orbits. The black contour lines show the result of thickening the disk by a factor of 2 in the direction perpendicular to the disk plane. For comparison with Figs. 1 and 4, we have superimposed the inner ellipse and a section of the outer ellipse displayed in those figures onto this diagram. The radial velocity contours are shown at intervals of 50 km s^{-1}. [*See the electronic edition of the Journal for a color version of this figure.*]

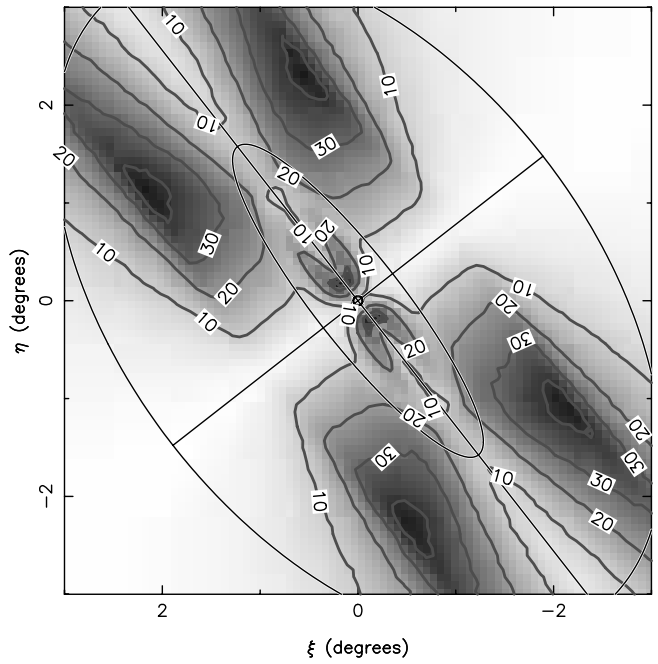

FIG. 8.—Since the Andromeda galaxy is observed close to edge-on, lines of sight through the disk can transverse a significant depth, unless the disk is infinitesimally thin. Here we illustrate the uncertainty caused by a 350 pc disk scale height on the circular velocity predictions displayed in Fig. 7. The contours show the levels where the uncertainty in the circular velocity model due to this disk thickness attains values of (from the outside in) of 10, 20, and 30 km s^{-1}. We include this additional error in when calculating the lag in velocity of stars behind the circular speed. However, over most of the survey region this additional uncertainty is less than 10 km s^{-1}. [*See the electronic edition of the Journal for a color version of this figure*.]

(*black lines*). The relatively small velocity offsets with respect to the gray-lined model show that the average projected velocity of circular orbits is not very sensitive to the assumed thickness of the disk.

Even though there is no intrinsic velocity dispersion built into this simple model (all matter moves in the plane of the disk in the direction tangential to the cylindrical radius coordinate with precisely the circular velocity), the thickness of the disk gives rise to a significant spread in the "observed" velocity. This is of course due to the fact that the line of sight intercepts matter at different galactocentric distances, where the density and also the projections of the velocity onto the line of sight are different. The map of the resulting apparent (rms) velocity dispersion is shown in Figure 8. For most of the survey area the additional uncertainty to the circular velocity model due to the intrinsic thickness of this flaring disk model is less than 10 km s^{-1}, although in certain regions the uncertainty is >30 km s^{-1}. We bear this consideration in mind when discussing the kinematic properties of the stars.

4.1. *Inner Fields*

We now proceed to present the velocity data. The top panel of Figure 9 shows the (heliocentric) radial velocity measurements as a function of x, the major-axis distance[7] for the disk fields labeled D1–D5 and which lie within the inner ellipse of Figures 1 and 4 (corresponding to a disk radius $R < 27$ kpc); a small number of stars from field F13 also fall into this selection. The dashed line here marks a heliocentric velocity of $v = -300$ km s^{-1}, the adopted systemic velocity of M31. Nonrotating populations such as might be expected for the stellar halo, will scatter in a broad distribution around this line. In these northeastern fields, the disk lies at radial velocities above the systemic value, so counter-rotating populations can be identified from their location below the dashed line. The bottom panel shows the result of subtracting the model of Figure 7 from the velocity data on a star-by-star basis (rather than using a single value for a whole field). Stars on circular orbits in the plane of the disk lie at a disk-corrected velocity of $v_{\rm lag} = 0$ (emphasized with a dashed line). Disk fields D1–D5 (located at major axis distances in the range 4 kpc $< x <$ 23 kpc) show a very similar distribution of stars, with a broad halo component below $v_{\rm lag} = -150$ km s^{-1}, and a well-populated peak lagging circular orbits only slightly. In Figure 10 we show the distribution of disk lag velocities for these fields, together with a Gaussian fit of the data in the range -150 km s$^{-1} < v_{\rm lag} <$ 100 km s^{-1}, which has a mean of $\overline{v}_{\rm lag} = -11$ km s^{-1} with dispersion of $\sigma_v = 54$ km s^{-1} ($\overline{v'}_{\rm lag} = -8$ km s^{-1}, $\sigma_{v'} = 61$ km s^{-1}). The dash-dotted line shows a similar maximum-likelihood Gaussian fit, this time taking into account the estimated velocity uncertainty on the individual velocity measurements, and also the uncertainty in the disk rotation model (from Fig. 8). This fit, which has $\overline{v}_{\rm lag} = -17$ km s^{-1} and $\sigma_v = 50$ km s^{-1} ($\overline{v'}_{\rm lag} = -15$ km s^{-1}, $\sigma_{v'} = 54$ km s^{-1}), shows that the dispersion of the population is not artificially enhanced to any significant extent by our line-of-sight depth through these fields.

As discussed above, contamination from Milky Way stars can be problematic for $v > -100$ km s^{-1}; however, the M31 disk has very high contrast in these inner fields (D1–D5), with a source surface density in our color-magnitude diagram (CMD) selection window that is 20 times higher than in the halo field F7, so we expect the Galactic contamination to be small, 5% at the very most. Thus we find that the dominant population in the inner regions of M31 is a thin-disk population with a dispersion of $\sigma_v =$ 49 km s^{-1} that trails circular orbits by $\overline{v}_{\rm lag} = -17$ km s^{-1}; these values are reasonably similar to the measurements of the velocity dispersion of the Galactic disk in the solar neighborhood, where the velocity ellipsoid has axes $(\sigma_R, \sigma_\phi, \sigma_z) = (38{:}24{:}17)$ km s^{-1} and the population lags the circular velocity with an asymmetric drift of $\sim$20 km s^{-1} (Dehnen & Binney 1998). Note that the very inclined orientation of M31 means that we do not have access to the vertical dispersion σ_z. The measured σ_v is a mixture of the radial and azimuthal components σ_R and σ_ϕ, dependent on the field under study. For simplicity we neglect this distinction in the present discussion, referring to a single σ_v.

4.2. *Outer Fields*

Having shown that the inner fields have kinematics typical of a canonical thin disk, we now examine the outer field data. The fields lying on the giant stellar stream (those prefixed by the letter S in Fig. 4) are removed from the sample for the sake of simplicity. This leaves a total of 16 fields marked F1–F16 in Figure 4.

The measured radial velocities in these fields are displayed as a function of major axis distance in the top panel of Figure 11. For clarity, we have removed from our sample all stars with heliocentric velocities $v > -100$ km s^{-1} (*small dots*), thereby minimizing the Galactic contamination (cf. Galactic model in Fig. 5). There is a wealth of kinematic substructure in these fields (S. Chapman et al. 2005, in preparation), and a significant halo population seen scattered around the systemic velocity (*dashed line)*; however, the dominant population in these fields again follows closely the disk rotation. This can be seen in the bottom

[7] We define the major axis distance as the distance from the minor axis toward the northeast parallel to the major axis.

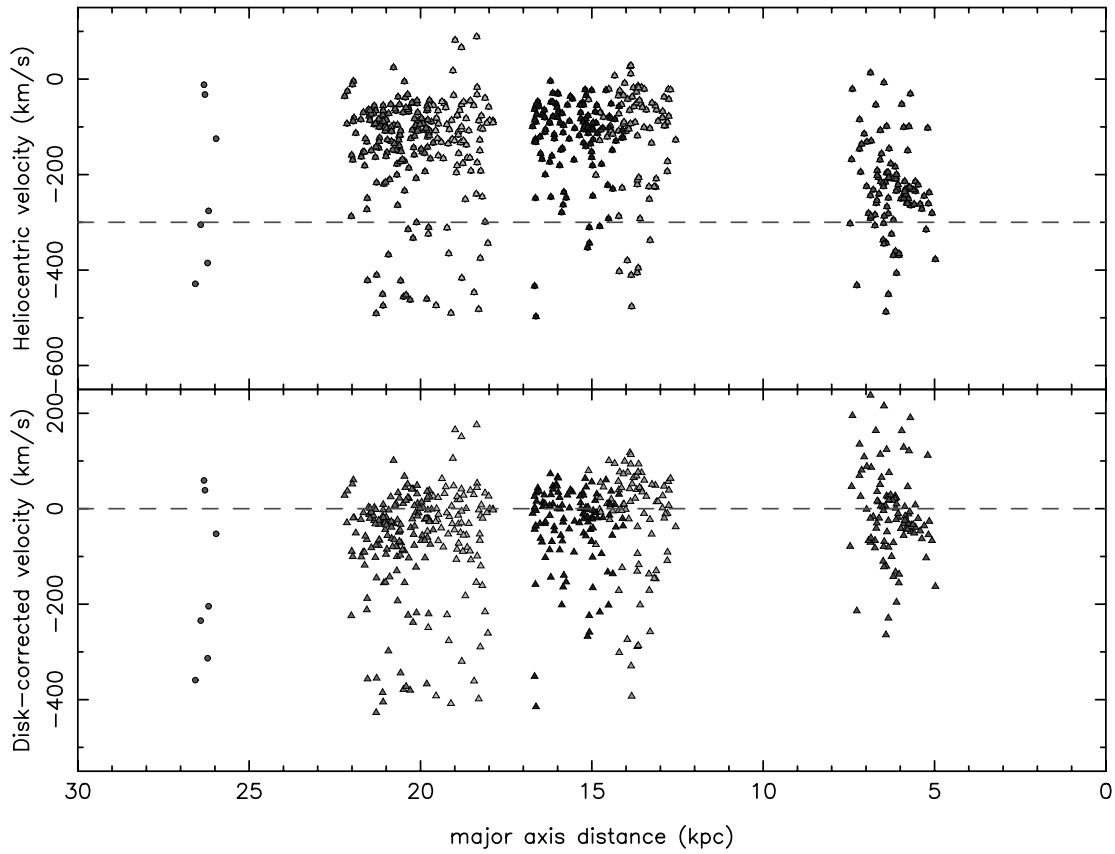

FIG. 9.—Radial velocity as a function of major axis distance for fields D1–D5 (with a few stars from F13 that lie within the inner ellipse of Fig. 4). The top panel shows the heliocentric radial velocity of the stars, with the dashed line marking the systemic velocity of M31. The bottom panel shows the same data "corrected" for the expected disk rotation given by the model shown in Fig. 7; now the dashed line marks the location of stars on circular orbits. The color coding of these data can be used to identify the corresponding field location in Fig. 4. [*See the electronic edition of the Journal for a color version of this figure*.]

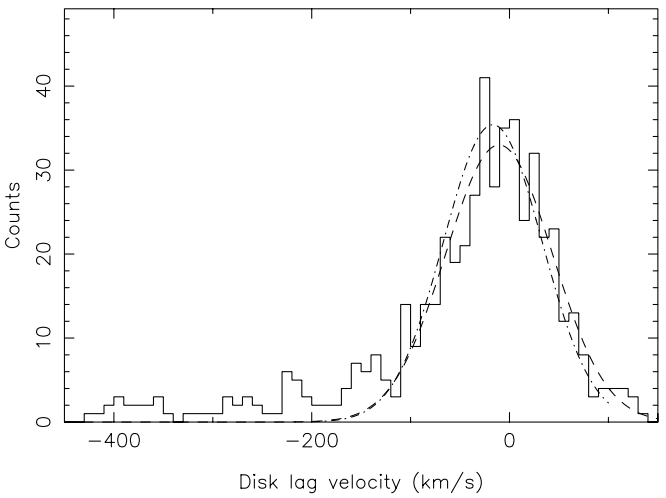

FIG. 10.—Summed distribution of velocity lags of fields D1–D5 (i.e., stars with major axis distances between 4 and 23 kpc in Fig. 9). The large peak in the range -150 km s^{-1} $< v_{\rm lag} <$ 100 km s^{-1} can be fitted with a Gaussian (*dashed line*) of mean $\overline{v}_{\rm lag} = -11$ km s^{-1} and dispersion $\sigma_v = 54$ km s^{-1} ($\overline{v'}_{\rm lag} = -8$ km s^{-1}, $\sigma_{v'} = 61$ km s^{-1}). The fit does not change significantly if we take into account the estimated velocity errors and the disk rotation model uncertainties displayed in Fig. 8, we obtain then (*dot-dashed line*) $\overline{v}_{\rm lag} = -17$ km s^{-1}, $\sigma_v = 50$ km s^{-1} ($\overline{v'}_{\rm lag} = -15$ km s^{-1}, $\sigma_{v'} = 54$ km s^{-1}).

panel of Figure 11, where we have corrected the data in the top panel for the rotation model of Figure 7. In the fields at major axis distance in the range -20 kpc $< x < -30$ kpc, the numerous population stands out clearly with "disk-corrected velocity" between -50 and 100 km s^{-1}. On this southwestern side of M31, positive velocities correspond to a lagging behind circular orbits. On the opposite side of the disk, at major axis distances $x > 5$ kpc, a similar concentration is found with "disk-corrected velocity" between -100 and 0 km s^{-1}. Here negative velocities lag behind the disk model.

For completeness, in Figure 12 we show the same velocity data as a function of minor axis distance, y.[8] It is clear from this diagram that the halo fields F5 and F7 (the two fields at minor axis distance $y < -15$ kpc) do not contribute significantly (if at all) to the peaked velocity structure that rotates as a disk.

Figure 13 shows the distribution of velocity lag $v_{\rm lag}$ in the 16 fields under consideration. The velocity lag is defined to be equal to the disk-corrected velocity for fields at positive major axis distance, but is inverted for fields at negative major axis distance. Each panel is labeled with the field name and three numbers, which give the major axis distance x, the minor axis distance y, and the deprojected M31-plane radius R, of the center of each field, all in kiloparsecs. A striking feature of these distributions is the presence of a narrow component in most of the fields, with mean velocity close to the circular velocity, that is to

[8] We define the minor axis distance as the distance from the major axis toward the northwest parallel to the minor axis.

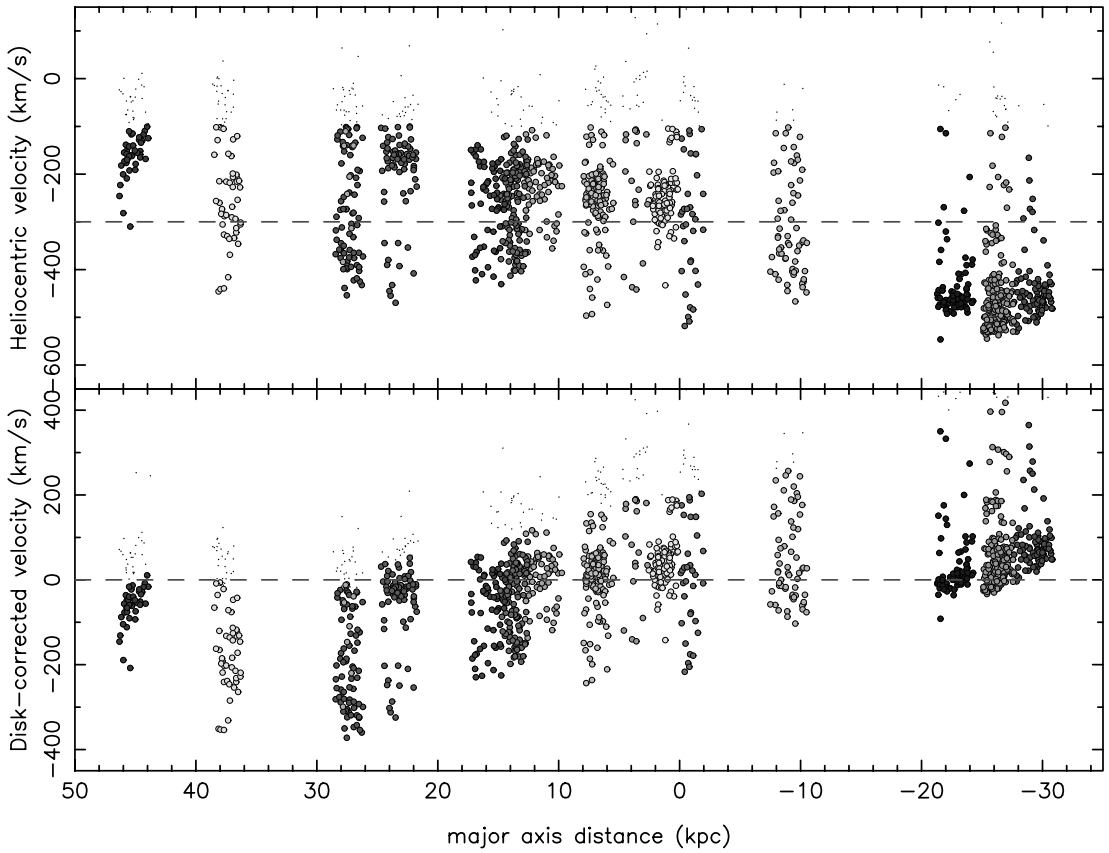

FIG. 11.—Same as Fig. 9, but for the 16 fields (F1–F16) that lie outside of the inner ellipse shown in Figs. 1 and 4, and which no not lie in the giant stream. In most of these fields the dominant population of stars is seen with velocities close to the expected mean velocity of circular orbits. Stars with heliocentric velocities $v > -100$ km s^{-1} lie in the velocity range where significant Galactic contamination is expected and are marked here with small dots. [*See the electronic edition of the Journal for a color version of this figure*.]

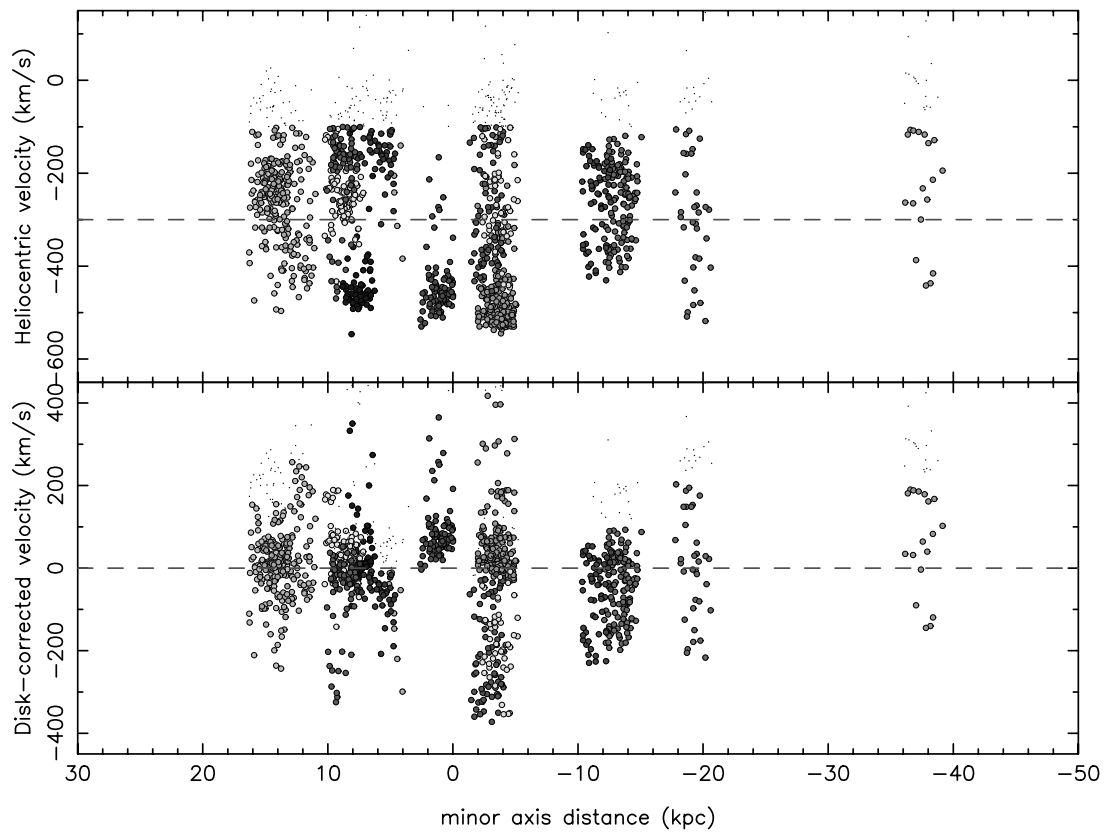

FIG. 12.—Same as Fig. 11, but showing the velocity as a function of minor axis distance. [*See the electronic edition of the Journal for a color version of this figure*.]

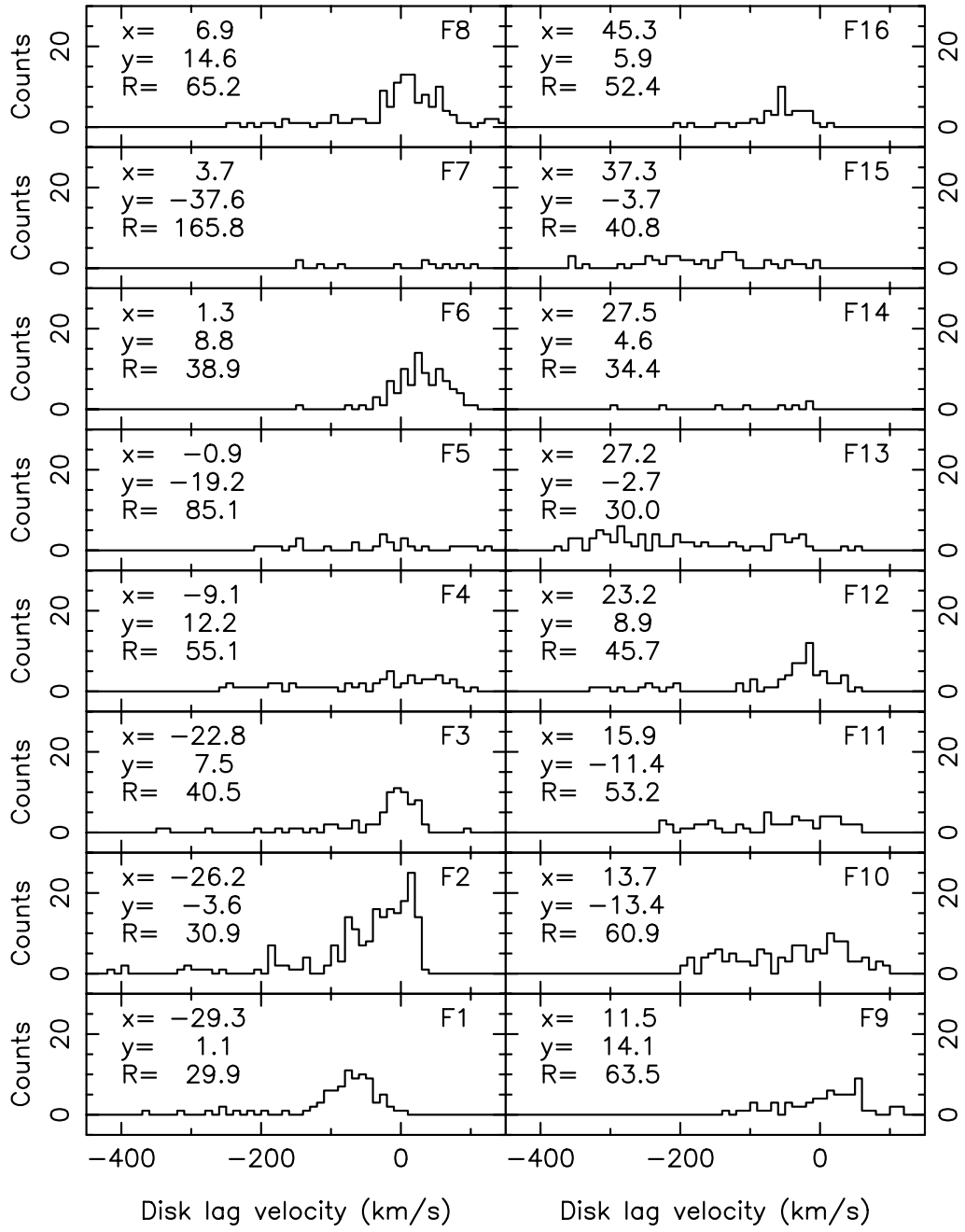

FIG. 13.—Distributions of the velocity lag behind the circular velocity model for the 16 fields displayed in Fig. 11. In each panel the three numbers show, respectively, from top to bottom, the major axis distance, the minor axis distance, and the deprojected radius R of the fields. The field name is also indicated.

say, a population that has distinctly disklike kinematics. Yet this is a startling finding, since these fields are extremely distant from M31, lying at radial distances between 30 kpc and more than 50 kpc. That this behavior is the most salient kinematic feature of the survey is demonstrated in Figure 14, which shows the distribution of velocity lag as a function of the M31-plane radial distance, R, for all stars in the survey in nonstream fields with $R < 80$ kpc. The majority of the stars are found with disk lag velocity in the range -100 km s^{-1} $< v_{\rm lag} <$ 50 km s^{-1}, and therefore take part in a large-scale rotational motion.

Summing the velocity lag distributions in all the outer nonstream fields (except for F6 to remove any concern regarding contamination from NGC 205—this will be discussed further in § 5.4) gives the distribution shown in Figure 15. This distribution is very similar to that previously constructed for the inner fields (cf. Fig. 10), showing again a broad halo distribution with the addition of a very strong peak, in this case centered at $\overline{v}_{\rm lag} = -16$ km s^{-1} with a dispersion of $\sigma_v = 51$ km s^{-1} ($\overline{v'}_{\rm lag} = -20$ km s^{-1}, $\sigma_{v'} =$ 45 km s^{-1}).

These data unambiguously show that the bulk of the stars in our survey fields share a common kinematic property: they corotate with the inner stellar disk, with velocities that lag circular orbits by $\sim$20 km s^{-1}, and possess a velocity dispersion of $\sim$50 km s^{-1}. There therefore appears to be a vast stellar disklike structure around the Andromeda galaxy, distributed on an unprecedented scale.

5. OVERVIEW OF SELECTED OUTER FIELDS

We next present in detail the data from seven of the outer fields, selected from Figure 13 for having a particularly strong

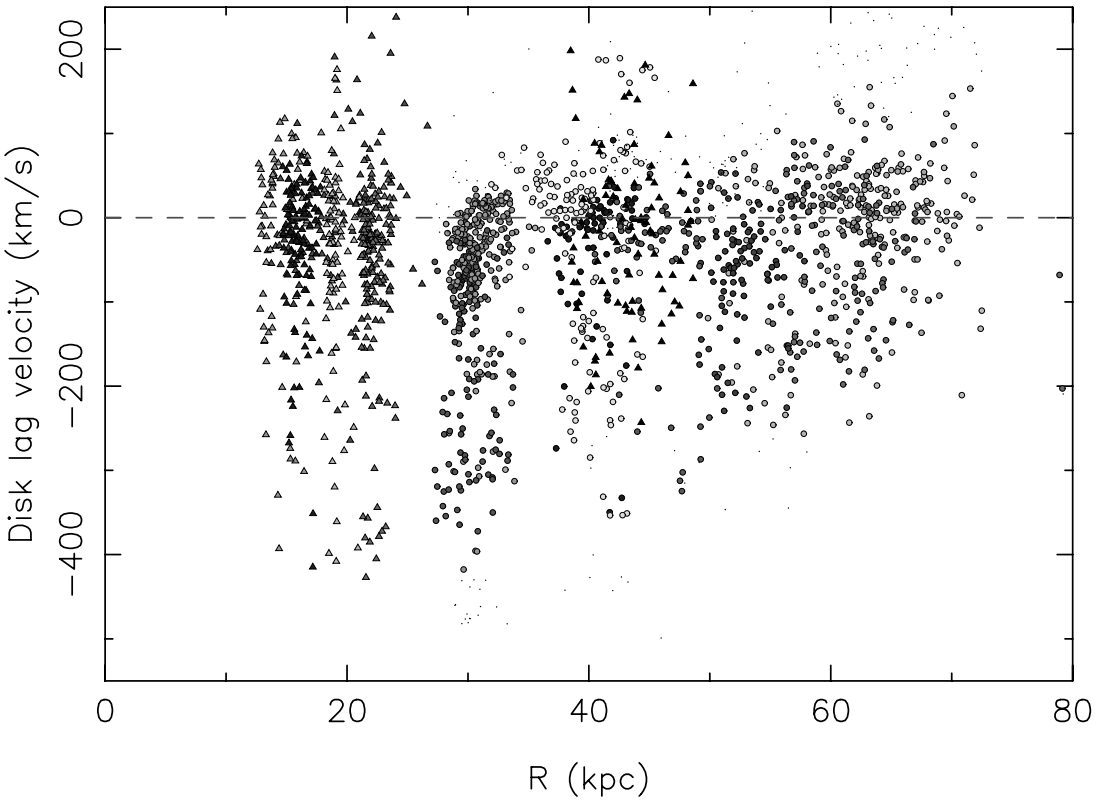

FIG. 14.—Distribution of velocity lags as a function of M31-plane deprojected radial distance in all nonstream survey fields at $R < 80$ kpc. Triangles mark the fields D1–D5, while circles mark fields F1–F16 (as in Fig. 11, small dots correspond to $v > -100$ km s^{-1}). The majority of these stars display small velocity lags (-100 km s$^{-1} < v_{\rm lag} < 50$ km s^{-1}) and are therefore rotating rapidly. The dashed line shows the location of circularly rotating stars. [*See the electronic edition of the Journal for a color version of this figure.*]

disklike peak in their velocity distributions. The selected fields are F1, F2, F3, F6, F8, F12, and F16.

5.1. *Field F1*

Field F1 lies at the southwestern boundary of the conspicuous dark and messy structure in Figure 1 that surrounds the bright inner disk seen in photographic surveys. The most massive of the M31 outer globular clusters, named "G1" also lies in this field, and we refer to the structure at this location as the G1 clump. We summarize the structural, kinematic, and photometric data on this field in Figure 16. The top left panel gives the location of the field with respect to the large survey area, which we zoom into in the top right panel. The bottom left panel shows the velocity distribution of the stars in our RGB selection window, together with a Gaussian fit centered at $\overline{v}_{\rm lag} = -68$ km s^{-1} with dispersion $\sigma_v = 30$ km s^{-1} ($\overline{v'}_{\rm lag} = -56$ km s^{-1}, $\sigma_{v'} = 31$ km s^{-1}). The bottom right panel shows the CMD derived from the INT survey over the $16.'7 \times 5'$ field of view of the DEIMOS instrument. Those stars with velocities within 2 σ of the mean of the Gaussian fit are marked with a filled circle. The four curves superimposed on this CMD are globular cluster fiducials, with metallicities, from left to right of [Fe/H] $= -1.91$, [Fe/H] $= -1.29$, [Fe/H] $= -0.71$, and [Fe/H] $= -0.2$. The stars that partake in the strong peak evidently scatter in a wide distribution around [Fe/H] ~ -0.7. Both the kinematics and the spectroscopic metallicity (presented in § 5.9) that we derive in this field are in excellent agreement with the findings of Reitzel et al. (2004).

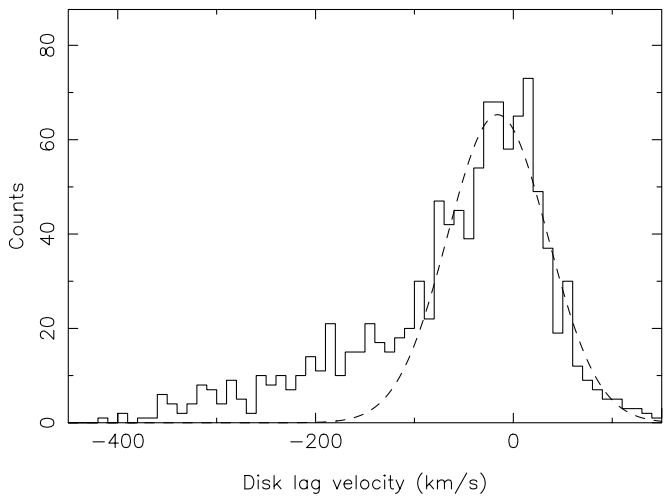

FIG. 15.—Summed distribution of velocity lags in all fields in Fig. 13 except F6. A Gaussian fit to the data in the range -150 km s$^{-1} < v_{\rm lag} < 100$ km s^{-1} is superimposed (*dashed line*), with a mean of $\overline{v}_{\rm lag} = -16$ km s^{-1} and a dispersion of $\sigma_v = 51$ km s^{-1} ($\overline{v'}_{\rm lag} = -20$ km s^{-1}, $\sigma_{v'} = 45$ km s^{-1}).

The spatial structure of this grouping of stars is very interesting. An inspection of the top right panel (and also Fig. 1) shows that this structure is an irregular lump—somewhat elongated east-west and apparently distinct from the disk. The structure is very large, being more than 10 kpc long. It is highly unlikely that this structure is bound, as this would require some $\sim 10^9\, M_\odot$ of dark matter, given the velocity dispersion and extent. Instead, the disorderly morphology argues in favor of this being tidal debris.

5.2. *Field F2*

Field F2 (Fig. 17) is located close to field F1, but in a prominence that descends southward of the disk. The velocity distribution in field F2 is similar to that of field F1, but contains

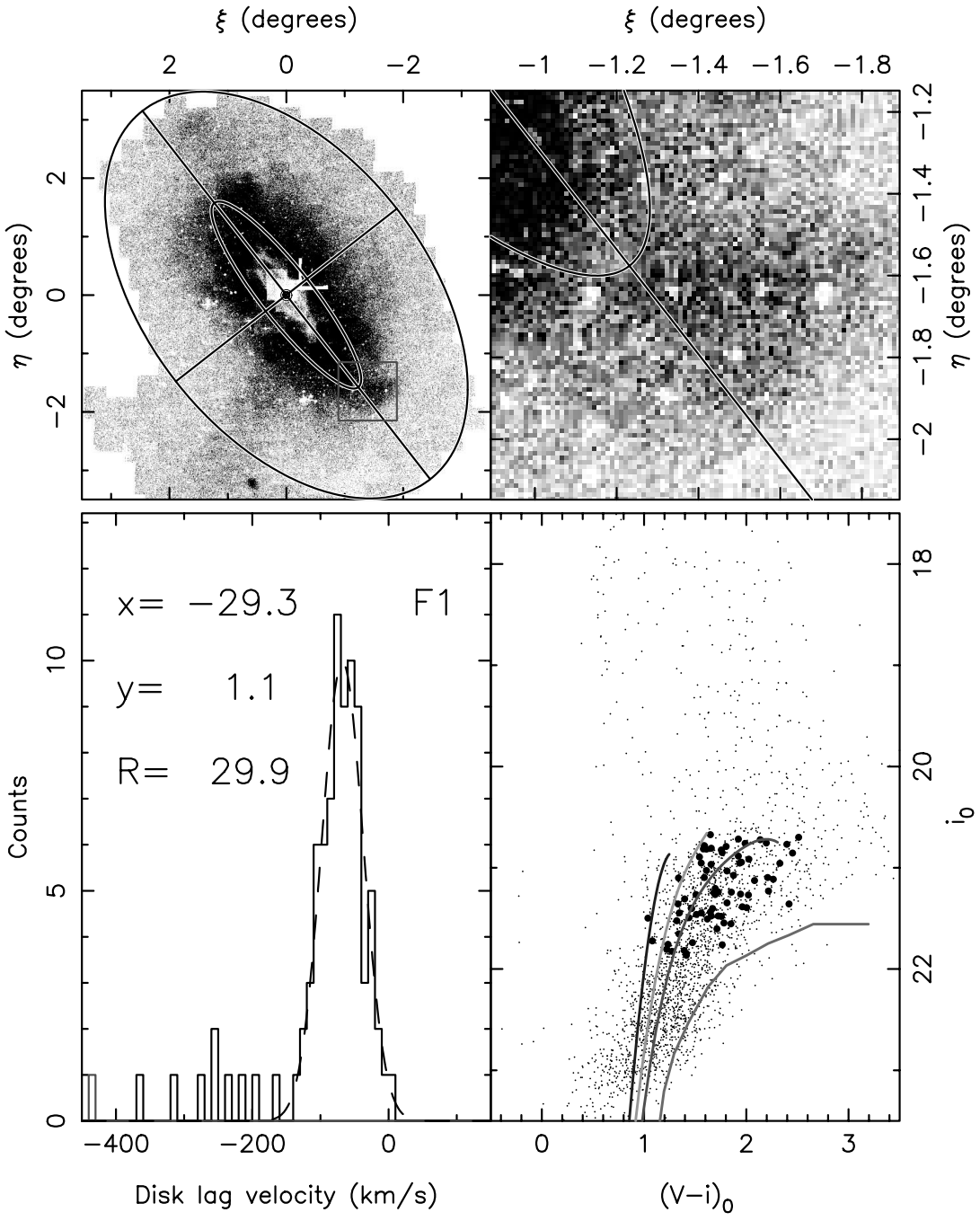

FIG. 16.—Top left panel shows the location of the field F1 in our survey region (compare to Fig. 1), with a $1^\circ \times 1^\circ$ box marking the location of the zoomed-in view displayed in the right, which is centered on the center of this DEIMOS field. The white holes present in this map are due to the halos of bright stars. The bottom left panel shows (*black*) the distribution of the velocity lag behind the circular velocity in this field, together with a single-component Gaussian fit, which has a mean of $\overline{v}_{\rm lag} = -68$ km s^{-1} and dispersion of $\sigma_v = 30$ km s^{-1} ($\overline{v'}_{\rm lag} = -56$ km s^{-1}, $\sigma_{v'} = 31$ km s^{-1}). The distribution of stars with heliocentric velocities $v > -100$ km s^{-1} are shown in the dotted histogram. The bottom right panel shows the CMD of the field, with small dots showing the full INT photometry within the area of the DEIMOS field of view. The filled circles are the stars with observed velocities within $\pm 2\ \sigma$ of the fitted Gaussian in the bottom left panel. For comparison, we have superimposed fiducial cluster sequences for (*from left to right*) NGC 6397, NGC 1851, 47 Tuc, and NGC 6553, which have metallicities of [Fe/H] $= -1.91$, [Fe/H] $= -1.29$, [Fe/H] $= -0.71$, and [Fe/H] $= -0.2$, respectively. [*See the electronic edition of the Journal for a color version of this figure.*]

an additional narrow component, which is seen as a spike near $v_{\rm lag} = 0$ in the bottom left panel of Figure 17. Fitting two Gaussian functions yields a narrow peak at $\overline{v}_{\rm lag} = 15$ km s^{-1} with dispersion $\sigma_v = 9$ km s^{-1}($\overline{v'}_{\rm lag} = 14$ km s^{-1}, $\sigma_{v'} = 5$ km s^{-1}), and a broader peak with $\overline{v}_{\rm lag} = -33$ km s^{-1} and $\sigma_v = 38$ km s^{-1} ($\overline{v'}_{\rm lag} = -25$ km s^{-1}, $\sigma_{v'} = 38$ km s^{-1}). The stars that give rise to the narrow kinematic spike are dispersed spatially over the whole DEIMOS field, so the structure is not simply a cluster. The small velocity dispersion and the mean velocity almost exactly on the expected circular rotation imply that the population is almost certainly young. The population in the broad kinematic peak is again very similar to the peak that we observe in field F1 and in the inner fields D1–D5.

5.3. *Field F3*

Field F3 is located toward the southwest of M31, on a dense elongated structure that trails behind the disk in a way that is reminiscent of a tidal stream or the end of a spiral arm (see Fig. 18).

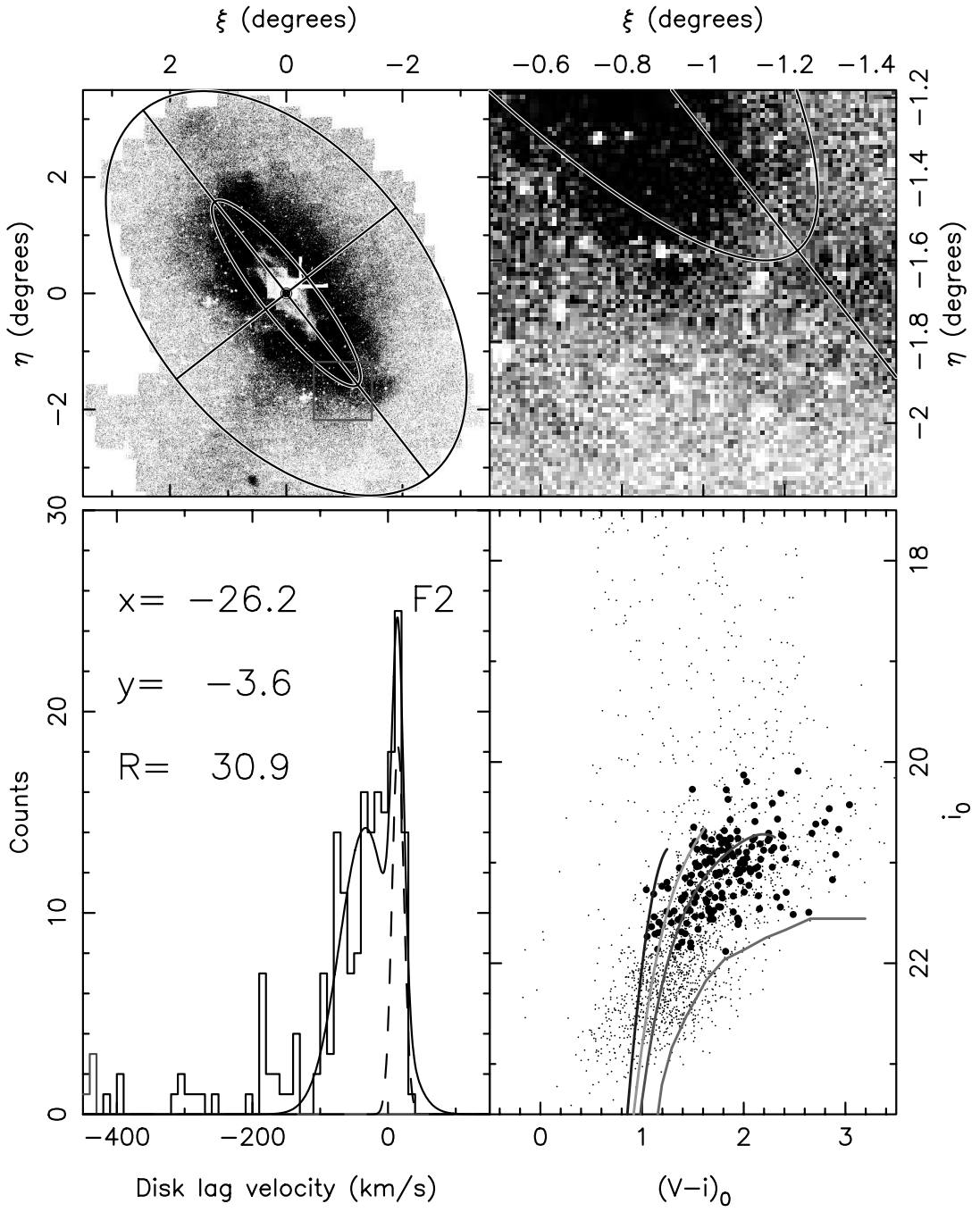

FIG. 17.—Same as Fig. 16, but for field F2. In this case we have fitted a two-component Gaussian model: we find a narrow peak centered at $\overline{v}_{\rm lag} = 15$ km s^{-1} with dispersion of $\sigma_v = 9$ km s^{-1} ($\overline{v'}_{\rm lag} = 14$ km s^{-1}, $\sigma_{v'} = 5$ km s^{-1}), and a broader peak with $\overline{v}_{\rm lag} = -33$ km s^{-1} and $\sigma_v = 38$ km s^{-1} ($\overline{v'}_{\rm lag} = -25$, $\sigma_{v'} = 38$ km s^{-1}). [*See the electronic edition of the Journal for a color version of this figure*.]

Although the velocity dispersion of $\sigma_v = 21$ km s^{-1} is relatively low in this field, the color-magnitude position of the stars that populate the kinematic peak is very similar to that seen in other fields.

5.4. *Field F6*

Figure 19 shows the velocity and color-magnitude data for field F6, centered on the northern edge of NGC 205, one of the dwarf elliptical satellite galaxies of Andromeda. The distribution of velocities has a narrow peak centered at $\overline{v}_{\rm lag} = 31$ km s^{-1} with dispersion $\sigma_v = 36$ km s^{-1}($\overline{v'}_{\rm lag} = 26$ km s^{-1}, $\sigma_{v'} = 35$ km s^{-1}). Surprisingly, this distribution is very similar to what has been found previously in other fields: the velocity dispersion is small and consistent with a circularly rotating population. Figure 20 displays the velocity and spatial data in more detail, with the middle panel showing the target positions with respect to a sketch of NGC 205. The top panel gives the heliocentric velocity measurements, while the bottom panel shows the velocity lag as a function of standard coordinate ξ. It is interesting to note that if some stars in this field were being removed from NGC 205 by the action of tidal forces, they would contribute, at least in projection, to stars with disklike kinematics; we return to this point in § 6 below.

5.5. *Field F8*

Figure 21 shows the data for field F8, a field in the possible tidal trail of NGC 205. This structure was discussed previously

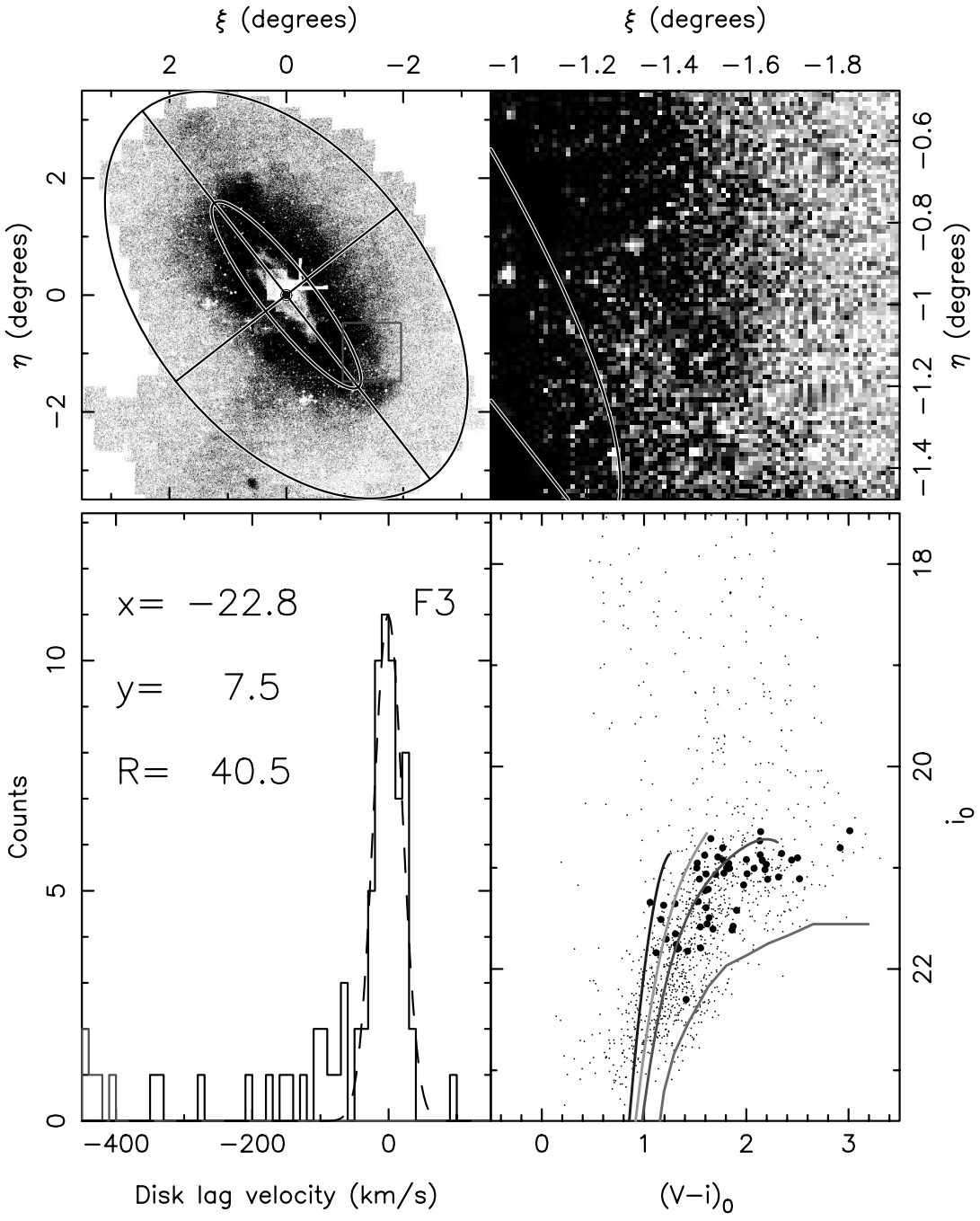

FIG. 18.—Same as Fig. 16, but for field F3. The Gaussian model has $\overline{v}_{\rm lag} = -1$ km s^{-1} and $\sigma_v = 21$ km s^{-1} ($\overline{v'}_{\rm lag} = -15$ km s^{-1}, $\sigma_{v'} = 17$ km s^{-1}). [*See the electronic edition of the Journal for a color version of this figure.*]

by McConnachie et al. (2004), who presented the morphology of the feature, together with kinematics from our field F9 (their field W91). The new data in field F8 (adjacent to field F9) do not show the bimodal distribution found by McConnachie et al. (2004), which suffered from a small sample size. Instead, the only significant stellar population present has, yet again, disklike kinematics with a dispersion of $\sigma_v = 36$ km s^{-1} centered at $\overline{v}_{\rm lag} = 14$ km s^{-1} ($\overline{v'}_{\rm lag} = 7$ km s^{-1}, $\sigma_{v'} = 35$ km s^{-1}).

5.6. *Field F12*

Figure 22 shows the location of another dense structure, this time located toward the northeastern end of the major axis. A peculiarity of this feature (the "Northern Spur") is its curious wedge-shaped morphology (seen in the top right diagram), which displays a very sharp boundary. The velocity dispersion of the structure $\sigma_v = 24$ km s^{-1} ($\sigma_{v'} = 23$ km s^{-1}) is again similar to that in other fields.

5.7. *Field F16*

Field F16 is situated in a particularly interesting location, on the northeastern end of our survey region (see Fig. 23), where our INT survey detected a very extended very low surface brightness structure. It lies at the greatest projected radius (46 kpc) of all the nonstream fields we observed. Zucker et al. (2004) argue that this

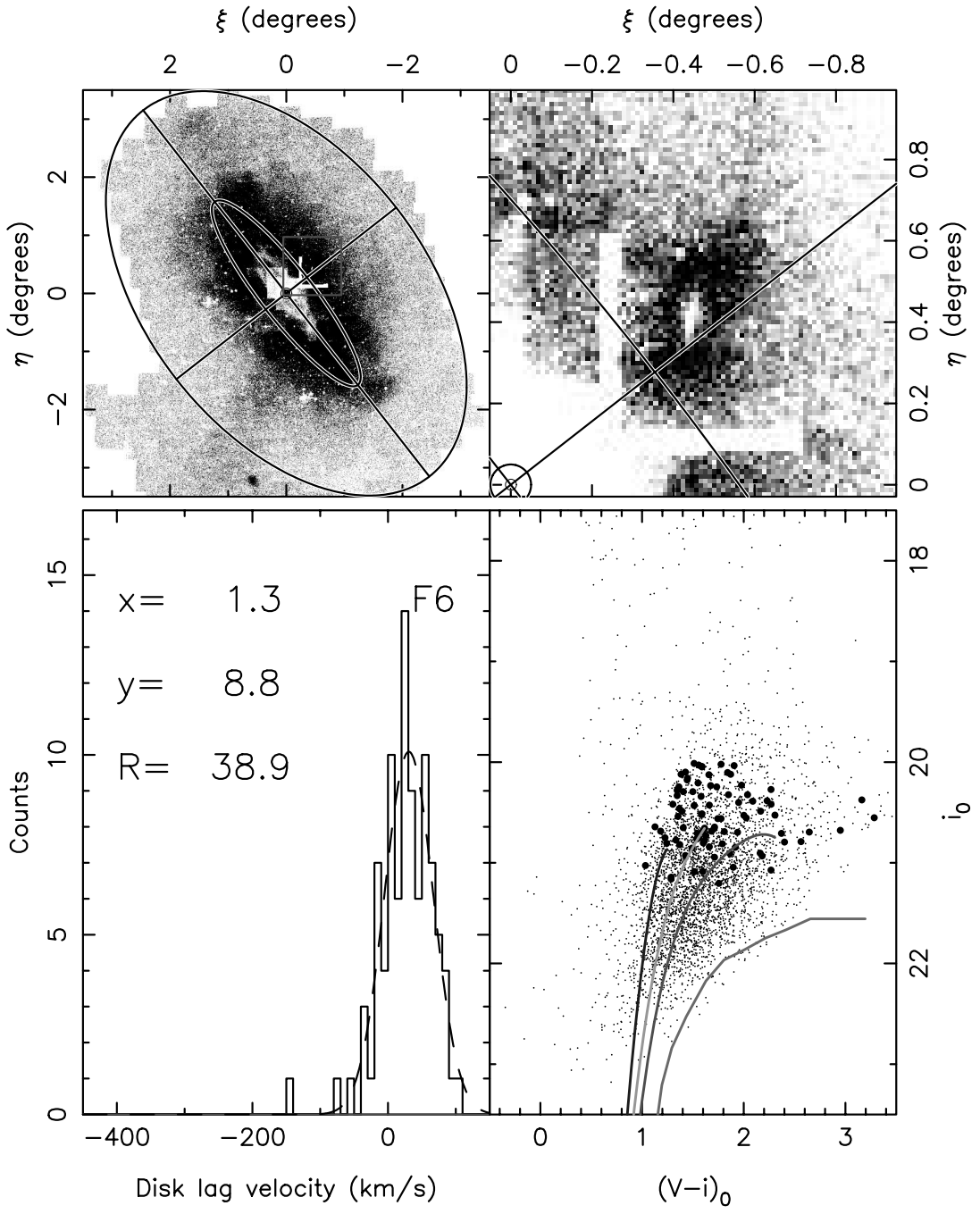

FIG. 19.—Same as Fig. 16, but for field F6. The Gaussian model has $\overline{v}_{\rm lag} = 31$ km s^{-1} and $\sigma_v = 36$ km s^{-1} ($\overline{v'}_{\rm lag} = 26$ km s^{-1}, $\sigma_{v'} = 35$ km s^{-1}). The white "L-shaped" hole in the finding chart is due to a deliberate shifting of the camera position to center one of the CCDs of the mosaic on NGC 205; part of the inner survey region was thereby not covered. The hole in the center of NGC 205 is a consequence of crowding. [*See the electronic edition of the Journal for a color version of this figure*.]

object (which they call Andromeda NE) may be one of the most low mass and low surface brightness galaxies found to date, or possibly torn-off material from the disk of M31. The radial velocity distribution in the bottom left panel of Figure 23 shows a well-defined narrow peak of dispersion $\sigma_v = 27$ km s^{-1} centered at $\overline{v}_{\rm lag} = -50$ km s^{-1}($\overline{v'}_{\rm lag} = -50$ km s^{-1}. $\sigma_{v'} = 31$ km s^{-1}). However, this field is the only one in our survey in which there could be some concern about Galactic contamination affecting significantly the fitted disklike peak. In Figure 24 we show the heliocentric velocity distribution of stars in this field, with the cut at $v = -100$ km s^{-1}, imposed on all fields to minimize the Galactic contaminants. The predictions of the Besançon Galaxy model are superposed (*light-gray histogram*) normalized to the $16.'7 \times 5'$ field of view of DEIMOS, but corrected for the ratio of available to observed targets in our CMD selection window. Thus, according to this model, below $v = -100$ km s^{-1} the Galactic contribution will be minor and can be neglected. The bottom right panel of Figure 23 shows the CMD location of the stars within the peak; evidently these are relatively metal-rich, and very similar to the other disklike stars found in the fields examined previously.

The velocity histogram in the bottom left panel of Figure 23 shows a spike at velocities -60 km s^{-1} $< v_{\rm lag} < -50$ km s^{-1}. The stars partaking in this spike are uniformly distributed over

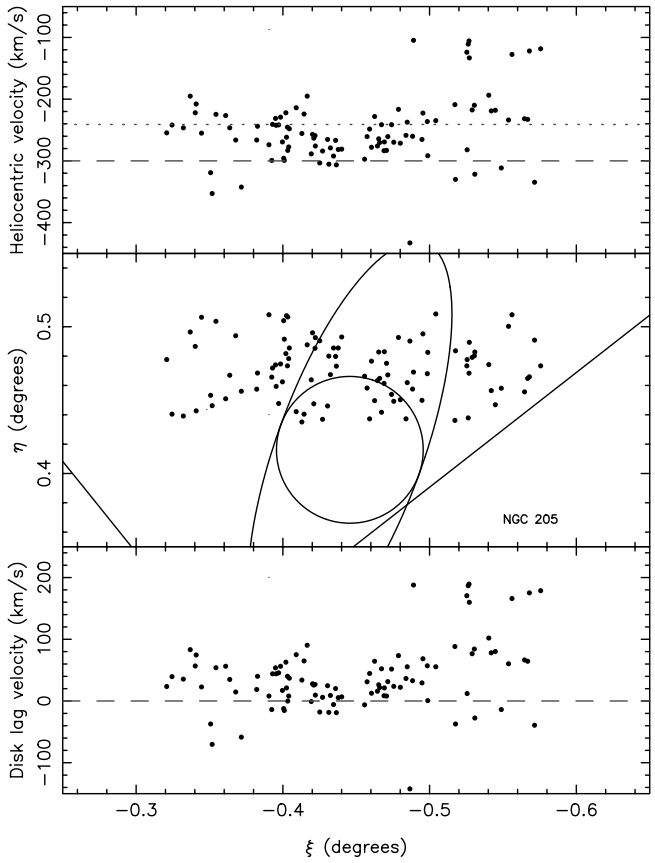

FIG. 20.—Central panel shows the positions of the targets in field F6 with respect to a sketch of NGC 205. The diagonal line segments show the minor and major axes of M31. The top and bottom panels show the kinematic data as a function of the standard coordinate ξ. The dashed line in the top panel marks the systemic velocity of M31, while the dotted line shows the systemic velocity of NGC 205. The bottom panel displays the corresponding distribution of disk lag velocity, with the dashed line marking the locus of circular orbits. [*See the electronic edition of the Journal for a color version of this figure*.]

the field, and they have a color spread similar to that of the other stars in the sample (the corresponding points are circled in the CMD in the bottom right panel). This lack of distinct properties, together with the low statistics, indicate that this spike is most probably an insignificant ($\sim 2\ \sigma$) random deviation.

Zucker et al. (2004) measure a radius of 6.6 kpc and a g-band absolute magnitude of -11.6 for this structure. If it were in Virial equilibrium, the velocity dispersion of $\sigma_v = 27$ km s^{-1} would imply a mass of $\sim 10^9\ M_\odot$, and mass-to-light ratio of $(M/L)_g \sim 160\ M_\odot/L_\odot$. This mass-to-light ratio value is extremely high and suggests that the object is more likely of tidal origin than a bound galaxy in dynamical equilibrium.

5.8. *Fields F4, F5, F7, F9, F10, F11, F13, F14, and F15*

The remaining outer nonstream fields—F4, F5, F7, F9, F10, F11, F13, F14 and F15—do not individually possess a narrow and strong velocity peak near the expected velocity of a circularly rotating population (see Fig. 13). However, by summing the fields together we can enhance the signal to detect a global population that lags the disk by a similar velocity. The nine fields that were added together cover a very large area over our survey. Some fields, in particular the halo field F7, are almost certainly devoid of any disk stars, so the "disk velocity lag" is not a meaningful quantity and will contribute only noise to the summed distribution. Nevertheless, Figure 25 shows that a narrow peak is again detected, albeit with a large population of "contaminants," this time stemming mostly from the halo population of M31 itself. Due to the kinematic substructure in the halo population (which will be presented in a forthcoming paper, S. Chapman et al. 2005, in preparation), we cannot easily remove the halo "contamination" to enhance the signal of the disklike peak. Nevertheless, to help guide the eye, we have used a maximum likelihood algorithm to fit a Gaussian function to the velocity data windowed in the range -100 km s$^{-1} < v_{\rm lag} < 100$ km s^{-1}, which we find to be centered on $\overline{v} = -7$ km s^{-1} with dispersion $\sigma_v = 57$ km s^{-1} ($\overline{v'}_{\rm lag} = -14$ km s^{-1}, $\sigma_{v'} = 52$ km s^{-1}). Although the reliability of this fit is clearly compromised by the strong halo contamination, the similarity of this peak with those presented in Figures 16–23 is very striking. This confirms that a disklike population is present in almost all the surveyed fields.

5.9. *Spectroscopic Metallicities*

The spectra also allow a measurement of the metallicity of the targeted stars from the equivalent widths (EWs) of the Ca II triplet absorption lines. While the noise in individual spectra is typically too high to yield a useful measurement of the Ca II equivalent widths, we proceeded to estimate the average metallicity by stacking the RGB star spectra of the targets within 2 σ of the fitted peaks of the fields displayed in Figures 16–23 (the corresponding stars are also highlighted in the CMD panels). The spectra are shifted to zero velocity before stacking. We follow as closely as possible the method of Rutledge et al. (1997), fitting Moffat functions to the Ca II lines. The average spectrum yields a measurement of the Ca II triplet equivalent width used to estimate the metallicity as $[{\rm Fe/H}] = -2.66 + 0.42[\sum {\rm Ca} - 0.64(V_{\rm HB} - V_{\rm ave})]$, with $\sum {\rm Ca} = 0.5{\rm EW}_{\lambda 8498} + 1.0{\rm EW}_{\lambda 8542} + 0.6{\rm EW}_{\lambda 8662}$, $V_{\rm HB}$ being a surface gravity correction relative to the V magnitude of the horizontal branch, and $V_{\rm ave}$ the average (luminosity weighted) magnitude of the stars in the field. We adopt the value of $V_{\rm HB} = 25.17$ for M31, measured by Holland et al. (1996). The resulting combined spectra are displayed in Figure 26, along with the metallicity measurement (on the Carretta & Gratton 1997 scale). The typical uncertainty is $\sim$0.2 mags. By chance, the λ8498 line in the summed spectrum in field 16 falls at the location of a night-sky line, so the two other Ca II were used in that instance. For comparison to the inner fields, in the top panel of Figure 26, we also display the summed spectrum of disk fields D2–D5, derived from those stars within 2 σ of the fit shown in Figure 10.

These metallicity measurements are all very similar, identical within the uncertainties, and agree reasonably well with the position of the targets relative to our fiducial clusters on the CMD. This yields further evidence that the dominant population in the majority of the fields we surveyed starting from the disk populations at a radius of 15 kpc out to $\sim$50 kpc are probing different parts of the same global population, which has a mean metallicity of $[{\rm Fe/H}] \sim -0.9$.

5.10. *Scale Length*

A further useful constraint on the nature of this disklike population is its density profile. We proceed by measuring the number n_s of stars within 2 σ of the narrow peaks shown in Figures 10 and 16–23, and count the number of observed targets n_o in the CMD selection window and the number of available targets n_t within the selection window that fall into the DEIMOS field of view. The local density in a field is estimated as $n_t n_s/n_o - n_b$, where n_b is the background density computed from fields

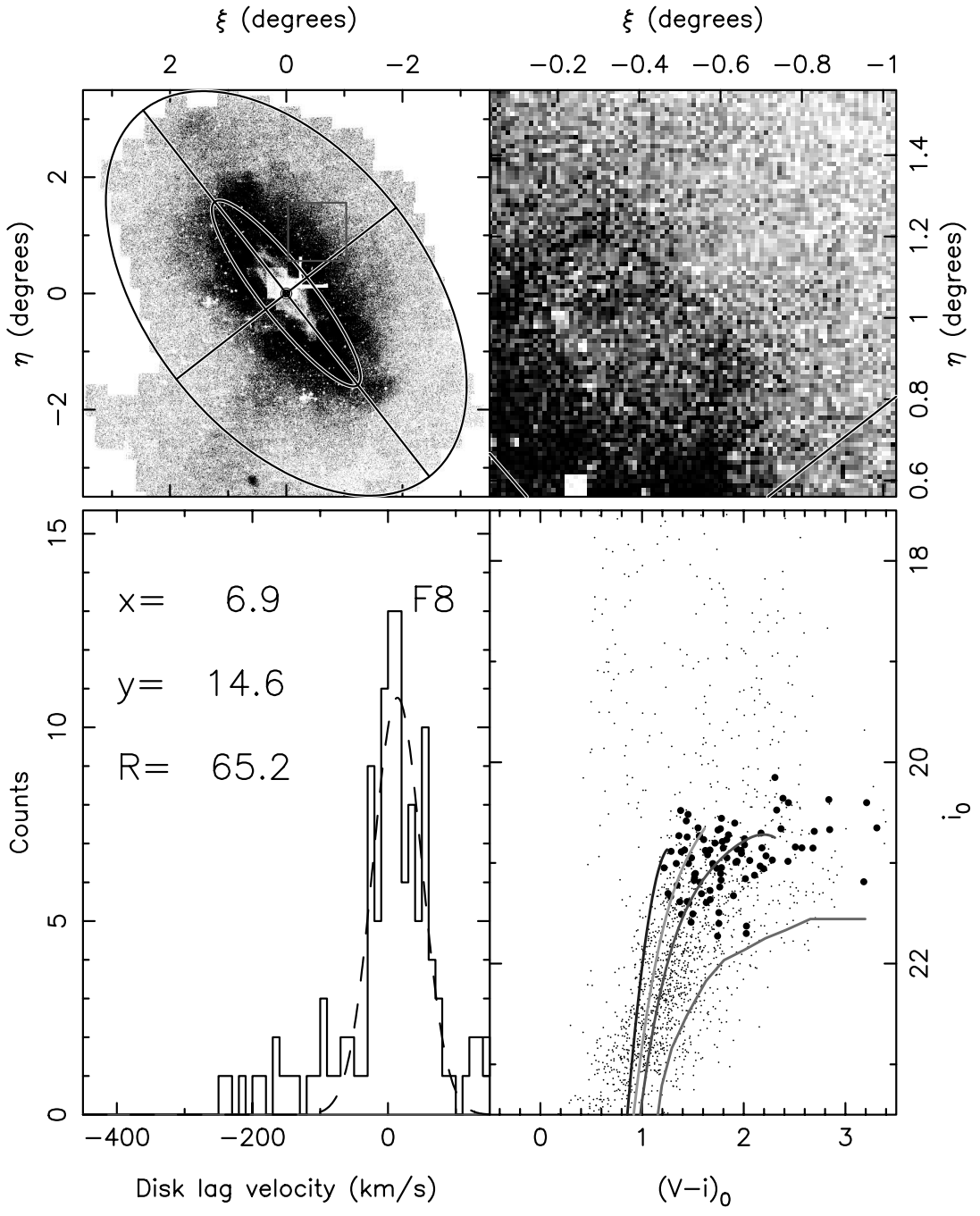

FIG. 21.—Same as Fig. 16, but for field F8. The Gaussian model has $\bar{v}_{\rm lag} = 14$ km s^{-1} and $\sigma_v = 36$ km s^{-1} ($\overline{v'}_{\rm lag} = 7$ km s^{-1}, $\sigma_{v'} = 35$ km s^{-1}). [*See the electronic edition of the Journal for a color version of this figure.*]

at the edge of the survey. The top panel of Figure 27 shows the resulting RGB star density profile, under the assumption of the standard Walterbos & Kennicutt (1988) inclination angle of $i = 77^\circ$. The profile shows an exponential decline to $R \sim 40$ kpc, at which point there appears to be a break in the relation, with possibly a flat extension from ~40 to ~70 kpc. Fitting the data at $R < 40$ kpc, we measure an exponential scale length of $h_R = 6.6 \pm 0.4$ kpc. This value is somewhat higher than the 5.1 ± 0.1 kpc scale length (*dotted line*) that we fitted earlier to the major axis star counts. If we instead assume the lower inclination angle calculated in § 2 of $i = 64.^\circ7$ (*bottom panel*), the scale length changes marginally to $h_R = 6.5 \pm 0.3$ kpc.

These longer scale lengths may mean that the population with disklike kinematics that we have uncovered in these fields has a slightly different profile to the underlying exponential population revealed in Figure 2, or it may also mean that the inclination of the outer disk is lower than $i = 64.^\circ7$. However, it should be recalled that the spectroscopic fields preferentially targeted overdensities detected in the photometric survey, which need not follow closely the medianed major axis profile. Another important property to bear in mind when interpreting Figure 27 is that the velocity distributions in all fields showed narrow peaks at a similar velocity lag. There was no indication of bimodal distributions with a component due to an underlying smooth "normal"

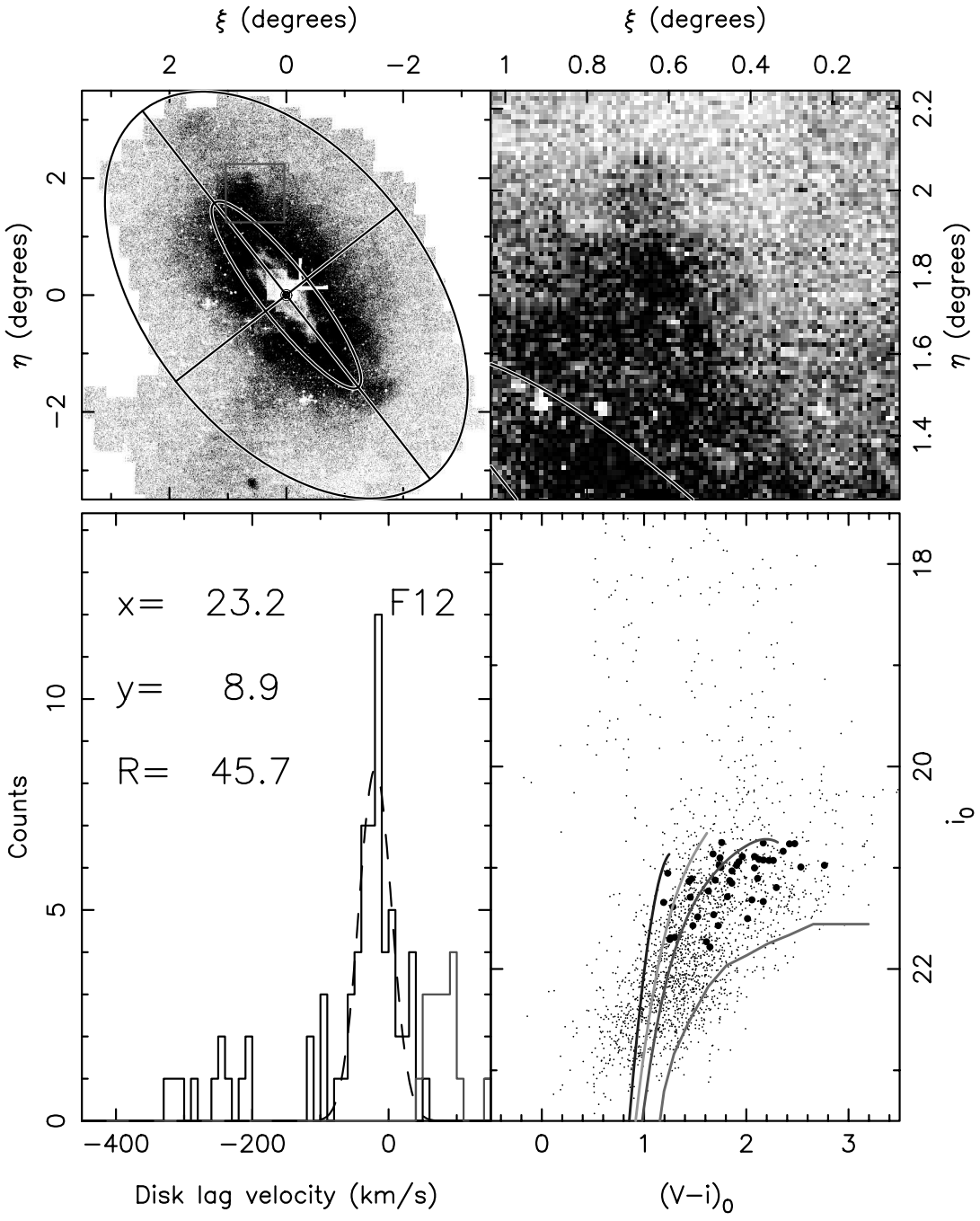

FIG. 22.—Same as Fig. 16, but for field F12. The Gaussian model has $\bar{v}_{\rm lag} = -20$ km s^{-1} and $\sigma_v = 24$ km s^{-1} ($\overline{v'}_{\rm lag} = -36$ km s^{-1}, $\sigma_{v'} = 23$ km s^{-1}). [*See the electronic edition of the Journal for a color version of this figure.*]

disk plus an additional component due to the substructure (with the exception of field F2 which we discussed in § 5.2). If there were an underlying normal disk population it has identical kinematics to the substructure.

5.11. *Total Luminosity and Angular Momentum*

In terms of its mass fraction, the outer disk is a very significant part of the galaxy. As we have shown in Figure 2, the exponential decline can be followed out to 40 kpc or 7.8 scale lengths. Approximately 10% of the mass of the M31 disk therefore lies beyond the typical 4 scale length cutoff (Pohlen et al. 2000). This region contains an even larger fraction of the angular momentum of the disk: assuming a flat rotation curve results in ~30% of the angular momentum of the disk residing beyond 4 scale lengths.

5.12. H I *Content*

Recently, Thilker et al. (2004) have presented an analysis of Green Bank Telescope λ21 cm observations of M31 and its environment. Their very high sensitivity of 2.5×10^{17} cm^{-2} within a beam size of 2 kpc allowed them to detect many low-mass H I clouds as well as an extended filamentary component. A careful inspection of their Figure 1, in which the H I data cube is presented, reveals a spatial overlap between the H I emission and our extended disk fields. Furthermore, the velocities of the H I gas coincide with the peaks of the extended disk velocity

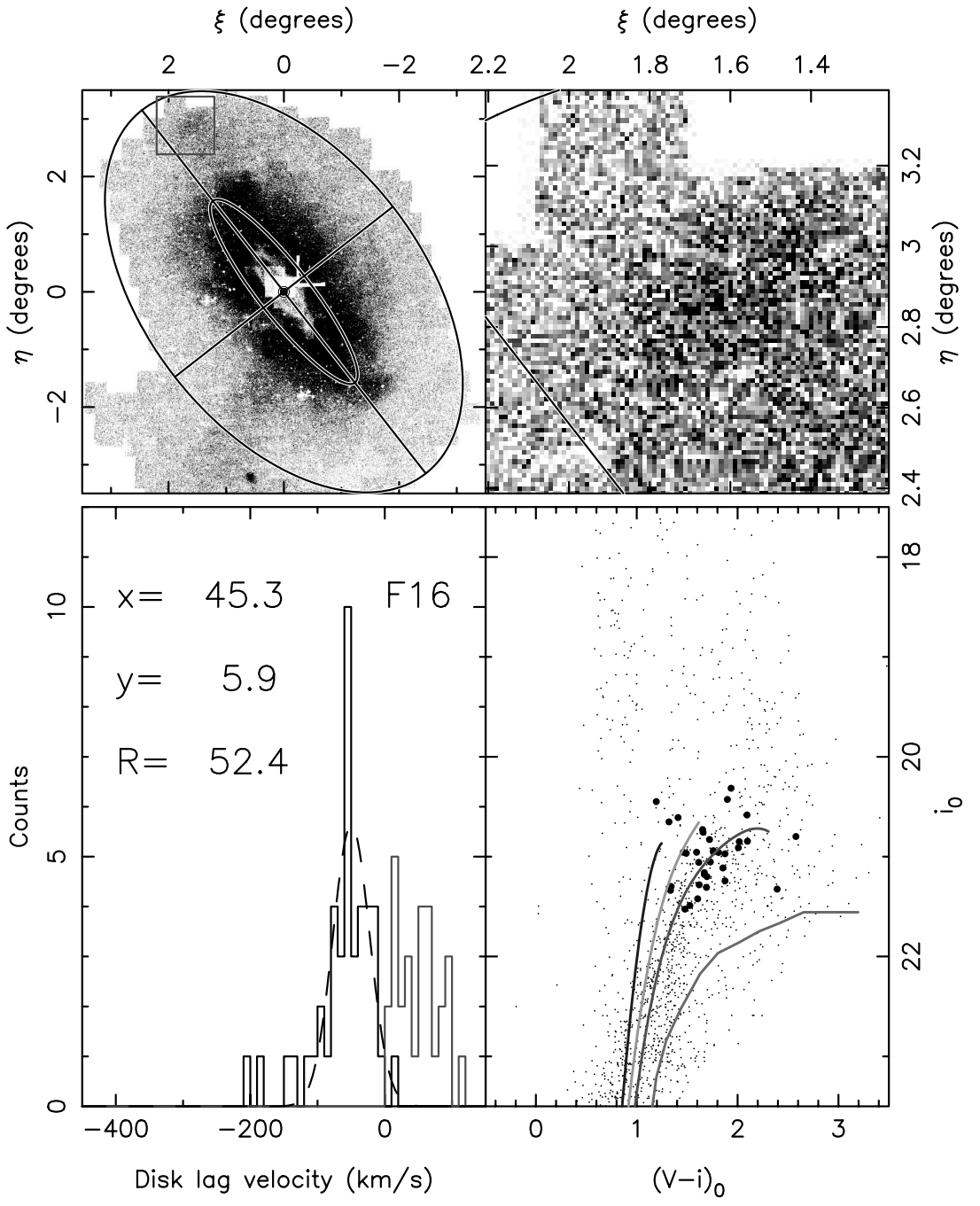

FIG. 23.—Same as Fig. 16, but for field F16. The Gaussian model has $\overline{v}_{\rm lag} = -50$ km s^{-1} and $\sigma_v = 27$ km s^{-1}($\overline{v'}_{\rm lag} = -50$ km s^{-1}, $\sigma_{v'} = 31$ km s^{-1}). [*See the electronic edition of the Journal for a color version of this figure.*]

distributions found in the present study, although a detailed comparison is not currently possible as the velocity intervals in the map presented by Thilker et al. (2004) are large (34 km s^{-1}).

5.13. *Variations in Stellar Populations*

The CMDs presented in Figures 16–23 show a very similar broad upper RGB, indicating that a similar distribution of stars populates these fields. However, recent work by our group (Ferguson et al. 2005) using very deep photometry from the Advanced Camera for Surveys (ACS) instrument on board the *Hubble Space Telescope* reveals significant differences in the morphology of the horizontal branch over the inner part of the M31 "halo." The surveyed fields include small areas of the fields F1, F5, F9, F10, F11, and F12 from the present study. The differences in the horizontal branch populations testify to the existence of inhomogenities in the *old* stellar populations in these fields.

6. DISCUSSION

Our radial velocity data reveal the presence of an unexpected population, present in almost all the surveyed fields from $R =$ 15 kpc out to ∼70 kpc, that lags the circular velocity by at most 70 km s^{-1}, and that has a dispersion of ∼20–∼40 km s^{-1}. This velocity dispersion is large enough to rule out the possibility that these structures are bound dwarf galaxies. It should be kept in mind that the circularly rotating disk model that we presented

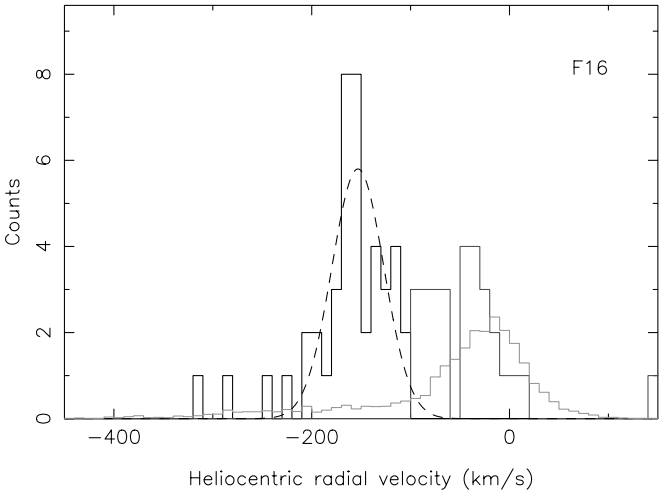

FIG. 24.—Heliocentric velocity distribution of field F16, situated in the low-surface brightness overdensity to the northeast of M31 (the data for $v < -100$ km s^{-1} is shown in black, whereas the region $v > -100$ km s^{-1}, which is likely contaminated by Galactic stars, is shown in dark gray). The light-gray histogram shows the prediction of the Besançon model in an area of the DEIMOS field of view, but corrected for the fact that only 92 stars in the CMD selection window were observed (out of a possible 282). The Besançon model therefore predicts that the Galactic contamination is minimal at heliocentric velocities $v < -100$ km s^{-1}, which strengthens the results presented in Fig. 23. [*See the electronic edition of the Journal for a color version of this figure*.]

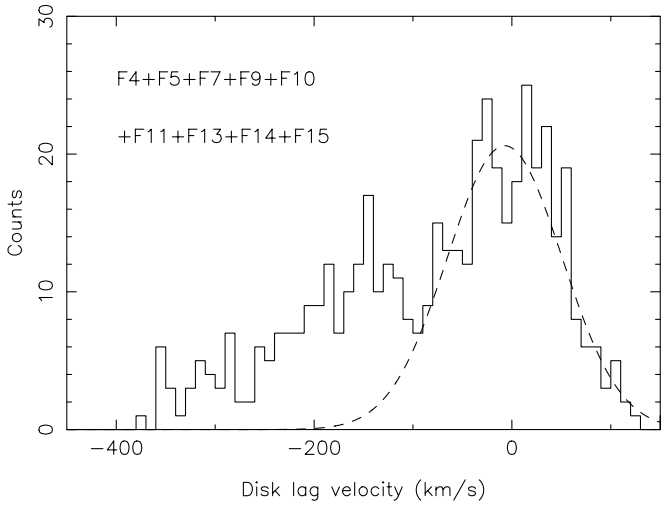

FIG. 25.—Distribution of disk lag velocities for the (nonstream) external fields without a prominent narrow disklike velocity component; these are F4, F5, F7, F9, F10, F11, F13, F14, and F15. This combining brings out of the noise, yet again, a narrow velocity peak close to expected velocity of a circularly rotating population. For illustrative purposes only, we have fitted the velocity interval -100 km s$^{-1} < v_{\rm lag} < 100$ km s^{-1} with a Gaussian of mean $\bar{v} = -7$ km s^{-1} and dispersion $\sigma_v = 57$ km s^{-1}($\bar{v'}_{\rm lag} = -14$ km s^{-1}, $\sigma_{v'} = 52$ km s^{-1}).

in Figure 7 is very simplistic, and one should expect significant deviations from it, especially on fields at large y (minor axis distance), where small changes in the inclination of the disk, due for instance to warping, will cause large errors in the disk velocity lag. So the good agreement in the mean velocity of the disklike peak in each field is all the more surprising. The direction of the effect is such that if the disk is warped so that it is seen less edge-on, the model of Figure 7 will overestimate the rotational velocity, and a population will appear to run ahead of circular motion.

The errors in the model, however, will not affect significantly the fitted σ_v in each field. The variations in σ_v in the outer fields are large, ranging between $\sigma_v = 21$ km s^{-1} in field F3 and $\sigma_v = 38$ km s^{-1} in field F2. Field F2 mirrors field F3 about the major axis, so we can see that the differences in velocity dispersion reflect real changes between fields, which are not just due to different projections of the R and ϕ components of the velocity ellipsoid onto the line of sight.

For the metallicity measurements we are unfortunately forced to co-add the spectra in the velocity peaks to obtain combined spectra with useful signal-to-noise ratios. This necessarily means that we lose all information on the metallicity dispersion of the populations. Nevertheless, the mean metallicity can be measured reliably, and the derived values in all fields are consistent with the data from each field being drawn from a global population of identical metallicity.

All the DEIMOS fields that we present in this paper except for fields F5 and F7 were positioned on regions of high target density in M31, which is seen as the dark black area in a visual inspection of Figure 1. This corresponds to a surface number density of stars of approximately 10^4 deg^{-2} in the RGB selection window defined in § 3. The panoramic view of the INT survey provides an invaluable complement to the spectroscopic results. Given the very similar velocity dispersions, disk velocity lags, and metallicities of the stars that we have identified, it is clear from an inspection of Figure 1 that these populations can be united in a single morphological entity: an extended disklike structure that has rather remarkable well-defined fragmented substructures at its outer edge.

6.1. *Timescale for Dissolution*

With typical sizes of ~5 kpc and velocity dispersions of $\sigma_v \sim 30$ km s^{-1}, the virial mass associated with the substructures we discuss in § 5 would have to be of the order of $\sim 10^9\ M_\odot$. However, the total luminosity of these substructures is very low, although this is a difficult quantity to measure given the irregular morphology and the difficulty of identifying their spatial limits. For the case of field F16, where the structure is well-separated from M31, the total luminosity is a mere $3 \times 10^6\ L_\odot$. Thus if these structures are bound, they require a ridiculous mass to light ratio of several hundred in solar units. They are instead most probably unbound structures dissolving in the global potential of the galaxy.

It is informative to estimate the lifetime of the structures if they are indeed unbound. In this case both the winding due to differential rotation and the velocity dispersion of the structure set a dissolution timescale. In a potential with a flat rotation curve of velocity v_c, an unbound structure at galactocentric radius R becomes smeared out by an extent equal to its initial size in a time R/v_c, i.e., in 170 Myr at $R = 40$ kpc for the case of M31 (taking $v_c = 240$ km s^{-1}). Alternatively, if we consider just the effect of the expansion of the stellar population due to its velocity dispersion unconstrained by self-gravity, with a velocity dispersion of ~30 km s^{-1}, a structure of size 5 kpc will double in size in 170 Myr, fortuitously the same time estimated before. These simple arguments give an order-of-magnitude estimate of the survival time of the structures and strongly suggest that they cannot be long-lived.

6.2. *Age of Population*

Brown et al. (2003) present extremely deep photometry with the ACS camera for a field on the minor axis of M31. The location of this field, indicated in Figure 4 with a small square, lies at a projected radius of only $y = -11.4$ kpc. The corresponding deprojected radius is $R = 53$ kpc, beyond the break in the surface

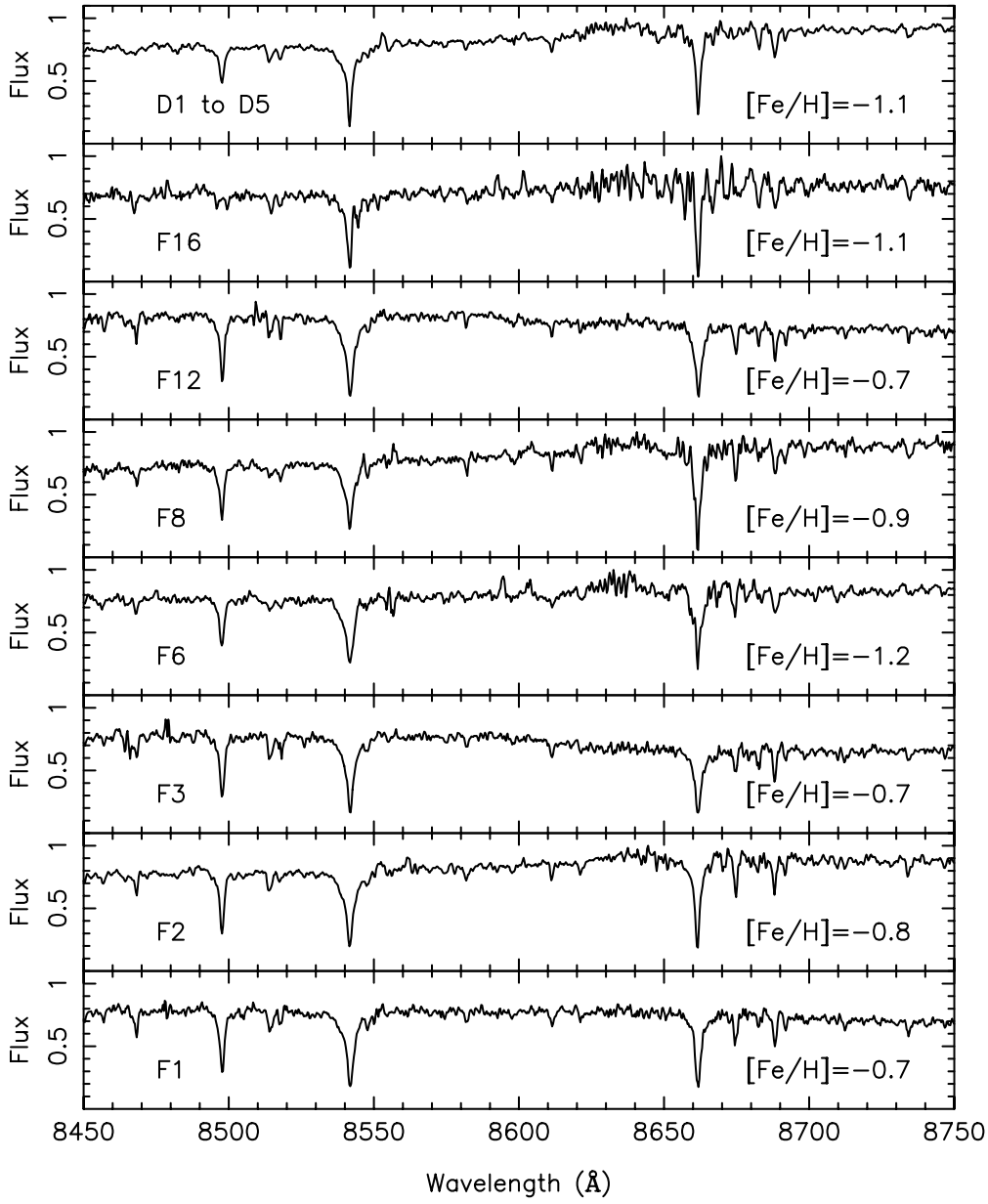

FIG. 26.—Combined spectra for all the stars within 2 σ of the Gaussian fit. The three Ca II triplet lines at 8498.02, 8542.09, and 8662.14 Å are the most obvious features of these spectra. The field name is indicated on the left, and derived metallicities on the right of each panel.

density profile of Figure 27. However, a tiny 5° warp in the extended disk would bring the field into the $R < 40$ kpc region. In their data, Brown et al. find evidence for a 30% component of intermediate age stars (6–8 Gyr) with metallicity $[Fe/H] > -0.5$, although they claim a similar quality fit for a population of metallicity $[Fe/H] > -1.0$. Given that this is the youngest component in that field and has comparable metallicity, it is possible that the intermediate-age population whose age they constrain is the extended disk. However, a definitive measure of the age of the population will require resolving the main-sequence turnoff in fields where we are sure that the extended disk population is present.

6.3. *Formation Scenarios*

The basic nature of the extended disk is currently not clear. It is possible that it is a series of tidal perturbations that simply happen to have disklike kinematics, in which case the structure would not be close to dynamical equilibrium, unlike stars formed in a classical stellar thin disk through the slow dissipational collapse of gas with ensuing star formation. Although this appears to be consistent with the deduction that the outer disk overdensities are transient features, it is curious nevertheless that the final end point configuration after these structures are smeared out perhaps ~1 Gyr in the future will be a smooth disklike structure.

Given this final outcome, it is tempting to speculate that disks may naturally have a significant fraction of accreted stars. This idea is supported by the hydrodynamic simulations of Abadi et al. (2003), who have shown that disks that grow in an ΛCDM cosmology can contain a small fraction (~15% in their simulation) of stars that were formed in satellite galaxies and were subsequently accreted. Given the high contrast of the outer disk features in M31 (these are typically 2–3 times denser than the background), it would be necessary for the accreted fraction to increase with radius so as to remain a small (~10%) fraction of the total disk.

Several possibilities for the formation of the extended disk present themselves.

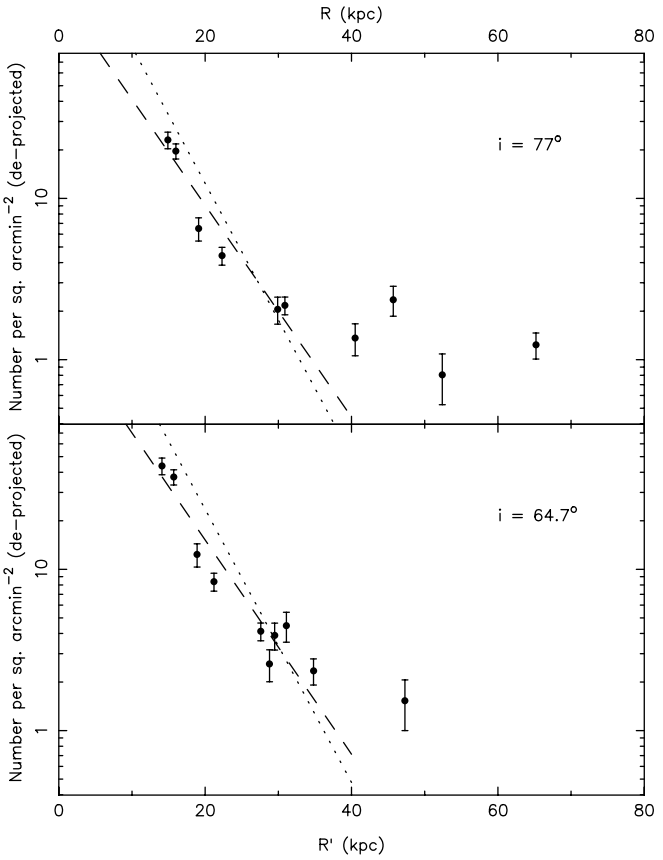

FIG. 27.—Density profile of the extended disk population is displayed in the top panel, isolated by counting kinematically confirmed stars and scaling by the ratio of possible targets to the total number of stars measured in each field. A disk-plane inclination of $i = 77^\circ$ is assumed to calculate both the deprojected radius R and the deprojected surface density. The dashed line shows an exponential fit to the data in the range $R < 40$ kpc, which implies a scale length of $h_R = 6.6 \pm 0.4$ kpc. The dotted line reproduces the fit to the outer major axis profile of Fig. 2 ($h_R = 5.1 \pm 0.1$). Field F6 is not included in this plot since it lies on the dwarf galaxy NGC 205, whose stars enhance enormously the number of possible targets in the DEIMOS field. The bottom panel shows the same data for $i = 64.^\circ7$. The fitted exponential function has scale length $h_R = 6.5 \pm 0.3$ kpc. The dotted line again reproduces the fit of Fig. 2, corrected for the difference in inclination angle.

1. *Formation by the accretion of many small subgalactic structures*.—This scenario would explain naturally the lumpy substructure seen at the edge of the extended disk, as well as the differences in the velocity dispersion and the variations in the old stellar populations between fields. However, the chemical homogeneity of the material argues against this possibility, since the different accreted galaxies would likely have a range of different metallicities, depending on their mass and star formation history. Admittedly, the metallicity measurements that we present above give only the mean of the population, and in the central regions of M31, considerable mixing must have taken place. Nevertheless, it is surprising to find the same mean abundance even in the outermost substructures. A further problem with this scenario is the disklike kinematics. A substantial mass is required for dynamical friction to affect the orbit of a galaxy satellite ($>10^8\,M_\odot$, Binney & Tremaine 1987), which has to become circularized *before* being disrupted in order to give rise to a final structure with disklike kinematics. Another problem is the disklike distribution of debris. Although accretion in the disk plane does appear to be favored (Peñarrubia et al. 2002), the accretion of a large number of halo objects is expected to give rise to a distribution closer to that of a spheroidal stellar halo than a disk. Even the thick disk component in the Abadi et al. (2003) simulation, in which ~50% is formed by accretion, is a very thick component of axis ratios ~1:3 and scale length of 4.5 kpc (our measurements from their Figs. 1 and 3). Forming the extended disk observed in M31 in this way will certainly be a challenge for modelers.

2. *Formation from stars accreted in a single large merger*.—Here we envisage the assimilation of a whole M33-sized galaxy in a single merging event. Accreting 10% of the total mass of a galaxy counts as a significant merger, affecting the morphology of the larger galaxy. However, given that the bulk of the interaction took place long ago, possibly 6–8 Gyr in the past (corresponding to $z \sim 1$), the progenitor of M31 would have been considerably less massive at that time (Hammer et al. 2005), and the resulting interaction would likely be termed a "major merger," after which Andromeda would have been globally reshaped. Thin disks are easily heated up by mergers (Tóth & Ostriker 1992; Velazquez & White 1999), so this scenario makes a testable prediction that stars in the inner disk of M31 that formed before the merger should have a much larger scale height than the younger thin disk. The advantage of this proposition is that it accounts naturally for the uniform mean abundances measured in the different fields.

Simulated mergers of disk galaxies typically give rise to end products that resemble ellipticals (Hernquist 1992, 1993), possessing $R^{1/4}$-law inner stellar profiles, but with rapidly rotating and flattened outer envelopes. This inner profile is precisely what is observed in M31 (Durrell et al. 2004), while the outer disk structure that we have uncovered may represent the rotating outer envelope of the merger remnant. Since M31 is evidently not an elliptical galaxy, this scenario would only appear plausible if the interaction took place before the formation of the bulk of the thin disk. However, this constraint may be weak: new simulations by Springel & Hernquist (2005) cast doubt on the inevitability of forming elliptical galaxies from diskdisk collisions, showing that disk galaxies may form even in equal mass mergers if the progenitors are gas dominated. Further numerical experiments are clearly required to establish whether a disk as extended as the one seen around M31 can be formed in this way.

3. *Formation induced by a single large merger*.—This scenario would be similar to the previous one, but the stellar population of the accreted galaxy would end up populating the bulge or other spheroidal component of M31. This is perhaps consistent with the presence of a double nucleus in that galaxy (Lauer et al. 1993). However, the interaction itself could have triggered star formation on a massive scale in the preexisting gaseous disk of M31, with gas accreted from the satellite contributing to the enrichment. This possibility could explain the disklike structure and kinematics, and it has the testable prediction that its constituent stars should be no older than the interaction itself. The homogeneity in mean abundance over the structure could be explained by star formation being limited very rapidly before chemical enrichment could take place. Such a rapid formation of the disk in this way is similar to what is deduced for ~1 mJy submillimeter sources at $z \sim 2$ with star formation rates of $\sim 100\,M_\odot\ \mathrm{yr}^{-1}$ (Chapman et al. 2003; Greve et al. 2005). Nevertheless, this scenario is also problematic, as it is hard to reconcile with the variations in the velocity dispersion between fields.

A concern with the last two scenarios is that the substructures that we see on the outskirts of the extended disk now are short-lived features that will soon disappear ($\ll 1$ Gyr). This means that we would be observing the system at a special time at the

very tail end of the merging process. A further problem is the constraint on the size of a past major merger set by the existence of a possible population of thin disk globular clusters that has recently been discovered in M31 by Morrison et al. (2004).

6.4. *Globular Clusters*

Morrison et al. (2004) infer that the existence of these old globular clusters with thin disk kinematics implies that no more than 10% of the mass of the disk could have been accreted in a single merger since their formation. The time of formation of the bulk of these clusters is currently poorly constrained, although they find no reason why they should be significantly younger than those of the Milky Way. However, subsequent studies of the disk clusters (Burstein et al. 2004; Beasley et al. 2004; Puzia et al. 2005) have found that many of the sample of Morrison et al. (2004) are in fact massive young clusters rather than old globular clusters. These findings weaken the constraint on the time since the last major accretion, although further studies are needed to establish the fraction of old globular clusters in the disk.

More recently, Fusi Pecci et al. (2005) have identified a population of massive globular clusters scattered around the outskirts of the inner disk at distances of $\sim$20 kpc. These objects have very blue colors, with color indices indicating a young age of $\sim$2 Gyr. The population is also very significant, accounting for $\gtrsim$15% of the globular cluster system of that galaxy. This population of young clusters rotates rapidly, possessing kinematics similar to that of the disk. A further piece of relevant information is provided by the recent discovery of the globular cluster Bologna 514 (Huxor et al. 2004; Galleti et al. 2005), which is situated close to the southwestern major axis of M31 at a projected distance of 55 kpc, almost exactly on the outer ellipse marked in Figures 1 and 4. The rotation model of Figure 7 gives a disk-lag velocity of this globular cluster of $v_{\rm lag} = -48$ km s^{-1}.

Though it is tempting to speculate on a possible connection between these globular clusters and the extended disk, the metallicities of the clusters appear to be much lower than the [Fe/H] $= -0.9$ we measure for the structures in this study. However, as pointed out by Fusi Pecci et al. (2005), the metallicities of these globular clusters could be higher if they are of younger age than the typical halo cluster. Further observations are needed to establish the age of these M31 disk clusters and their relation to the extended disk.

6.5. *Possible Connection to NGC 205?*

As we noted in § 5.4, if stars become unbound from NGC 205, we would observe them in field F6 with kinematic properties very close to that of disk material. Likewise, if McConnachie et al. (2004) were correct in identifying the arclike structure to the north of M31 as a tidal stream from NGC 205, this tidal debris, which is located in fields F8 and F9, would also have disklike kinematics.

This raises the possibility that NGC 205 is connected to the extended disk structure, either as the direct supplier of stars, or as the remnant of the ancient structure that created the extended disk. It is interesting to note in this context that the mean metallicity of NGC 205 has been measured to be [Fe/H] ~ -0.9 (Mould et al. 1984), identical to the mean spectroscopic measurements from the fields presented in this survey.

A counterargument however, is that recent estimates for the distance to NGC 205 indicate that it is behind M31, being at a distance of 824 ± 27 kpc (McConnachie et al. 2005), compared to $785 \pm 25 - 40.6 \sin i$ kpc for the M31 disk at the location of NGC 205. The difference in distance is therefore 79 ± 37 kpc, little over 2 σ, although we are probably grossly overestimating the uncertainties, since a differential distance measurement is expected to be much more accurate.

However, this need not rule out the connection with NGC 205. If the dwarf galaxy were indeed $\sim$80 kpc beyond the foreground disk on the near side of M31, it would be $\sim$40 kpc behind M31, at a location $\sim$17 kpc above the plane of the disk on the far side of that galaxy.

6.6. *Comparison to Hurley-Keller et al. (2004)*

Hurley-Keller et al. (2004) have presented an analysis of the kinematics of 135 planetary nebulae in the disk and inner halo of M31. They find the surprising result that a standard model for the thin disk, thick disk, and bulge cannot reproduce the observed planetary nebulae (PNe) kinematics at major axis distances of 15–25 kpc. In order not to introduce the presence of an additional component, they invoke Occam's razor to alter the parameters of the bulge, deducing that the bulge must rotate rapidly at large distances. We reassess their data in the light of the discovery of the additional extended disk population. Figure 28 shows the positions of the 135 PNe in their survey. Stars close to the center of M31 are a complex mix of populations, so we investigate the subsample with $|x| > 15$ kpc, which are displayed as filled circles for $R < 25$ kpc and as filled triangles for $R > 25$ kpc. The distribution of velocity lags for the two subsamples are shown in Figure 29. We fit these distributions using a maximum-likelihood algorithm, to account for the velocity measurement uncertainties quoted by Hurley-Keller et al. (2004), as well as the disk model uncertainties (from Fig. 8). The resulting Gaussian model has $\bar{v}_{\rm lag} = -34$ km s^{-1} and $\sigma_v = 49$ km s^{-1} for the inner sample and $\bar{v}_{\rm lag} = -12$ km s^{-1} and $\sigma_v = 51$ km s^{-1} for the outer sample, values that are very similar to the fit in Figure 10. Further analysis is necessary to establish conclusively whether the existence of the extended disk alleviates the need for a rapidly rotating outer bulge, as suggested by Hurley-Keller et al. (2004).

6.7. *A Connection with the Thick Disk?*

Several edge-on galaxies have been found to possess a flattened component with a much larger scale height than the thin disk (Dalcanton & Bernstein 2002), probably indicating the presence of a thick disk. Recently, two of the sample of Dalcanton & Bernstein (2002) were observed spectroscopically by Yoachim & Dalcanton (2005), who found the thick disk to be rotating very slowly in one case and counterrotating in the other. This result shows that thick disks can have completely different kinematics from the thin disk, although this is not the case for the Milky Way. The fact that the extended disk we find around M31 has a low velocity dispersion and follows circular orbits closely, thus behaving kinematically like a thin disk, as well as having a very similar scale length to the thin disk, suggests a close link with that component and argues against association with the thick disk of Andromeda. It should be noted, however, that it has not yet been shown that Andromeda does indeed possess a thick disk. The present data set may allow us to detect the thick disk, but we will return to this issue in a future contribution.

6.8. *Extended Disks in Other Galaxies?*

Our group has also been attempting to unravel the formation history of the Milky Way (Ibata et al. 2001b, 2002), with goals similar to those of to our study of M31. Following up on the discovery of a peculiar halo structure in the Sloan Digital Sky

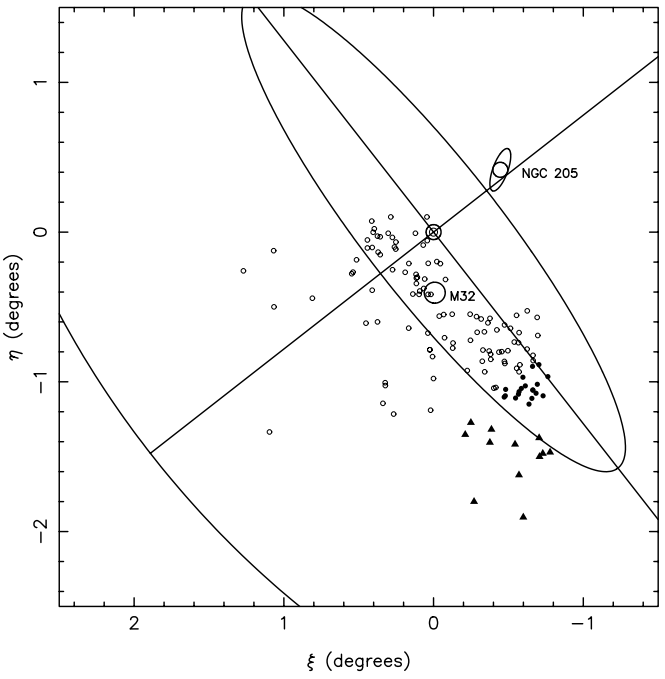

FIG. 28.—Location of the PNe from Hurley-Keller et al. (2004) with respect to M31; the lines and ellipses from Figs. 1 and 4 are reproduced to show the scale. The filled circles show the chosen subsample with $|x| > 15$ kpc and $R < 25$ kpc, filled triangles mark those stars with $|x| > 15$ kpc and $R > 25$ kpc, and open circles show the remaining data.

Survey (Newberg et al. 2002), we showed that the Milky Way is enveloped in a ringlike distribution of old stars that lie at Galactocentric distances of ~20 kpc, well beyond the edge of the Galactic disk (Ibata et al. 2003). A subsequent analysis of asymmetries in the Two Micron All Sky Survey revealed a strong enhancement of stars at the edge of the Galactic disk, which we interpreted as an accreted dwarf galaxy fragment (Martin et al. 2004a, 2004b; Bellazzini et al. 2004; see also Rocha-Pinto et al. 2005); a connection with the ringlike structure is possible, although not proven. However, this "Galactic ring" or "Galactic anticenter stellar structure" (Crane et al. 2003) is not the only stellar population with disklike kinematics that lies beyond the rim of the Milky Way thin-disk: recently Majewski et al. (2004) and Rocha-Pinto et al. (2004) have uncovered a further stellar structure located at a distance of ~40 kpc and which spans a huge angle on the sky. These findings indicate that the outer regions of the Galactic plane have a similar messy flattened structure to what is observed in M31 (Fig. 1).

A possible young counterpart to the "extended disks" in the Milky Way and M31 has been seen in some more distant galaxies. *GALEX* (*Galaxy Evolution Explorer*) observations of M83 (Thilker et al. 2005) have revealed an extended population of UV sources (OB stars) beyond the inner disk (although at much smaller radius than the structure we detect in M31), while several galaxies are known to exhibit H II regions to extremely large radii (Ferguson et al. 1998). Thus it appears that there may exist an additional component to spiral galaxies, a putative "extended disk." The implications for galaxy formation are profound: the inhomogenous spatial distribution and moderately high metallicity suggests an origin in multiple accretions, yet accreted fragments, which are the building blocks of galaxies, do not give rise to these huge extended disks in current simulations.

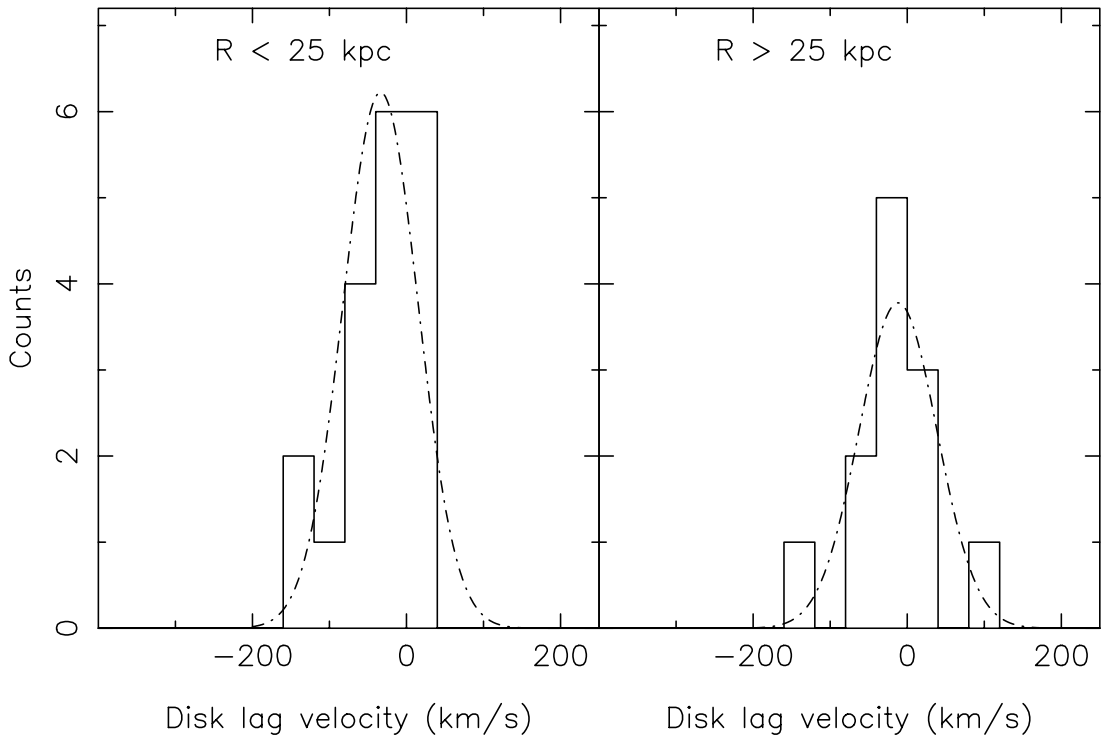

FIG. 29.—Distribution of disk lag velocities of the Hurley-Keller et al. (2004) PNe with $|x| > 15$ kpc, for $R < 25$ kpc (*left panel*) and $R > 25$ kpc (*right panel*). Maximum-likelihood Gaussian fits to the data are also shown, in which both the estimated velocity uncertainties from Hurley-Keller et al. (2004), as well as the uncertainties in the disk rotation model (from Fig. 8), have been taken into account. For the $R < 25$ kpc subsample, we fit a Gaussian mean velocity lag of $\overline{v}_{\rm lag} = -34$ km s^{-1} and dispersion $\sigma_v = 49$ km s^{-1}, while for the $R > 25$ kpc subsample we find $\overline{v}_{\rm lag} = -12$ km s^{-1} and dispersion $\sigma_v = 51$ km s^{-1}. The same low dispersion disklike population as discovered in our DEIMOS fields is also present here.

7. CONCLUSIONS

We have presented an analysis of a large survey of the Andromeda galaxy with the Keck DEIMOS spectrograph based on targets selected from a panoramic survey with the INT Wide Field Camera. A huge rotating structure that follows an exponential density law with scale length 5.1 ± 0.1 kpc is detected out to a deprojected distance of $\sim$40 kpc, with substructures continuing out even further in radius. All of the photometric substructures that were targeted for spectroscopic follow-up participate in the same disklike movement. The velocity dispersion in individual fields is low, typically 30 km s^{-1}. These properties indicate that the population is a huge extended stellar disk. This is consistent with a recent analysis by Worthey et al. (2005), who posited the existence of an extended disk around M31 to explain the metal-rich abundance distributions derived from *Hubble Space Telescope* photometry data in fields up to 50 kpc.

Indeed, our INT photometry shows that the color dispersion on the RGB of stars that belong to this structure is broad, implying that a wide metallicity range is present. Spectroscopic measurements of the mean metallicity give $[\mathrm{Fe/H}] = -0.9 \pm 0.2$. No significant radial trend in either kinematics or metallicity is found, although deep ACS photometry (Ferguson et al. 2005) in several of the DEIMOS fields reveals variations in the horizontal branch morphology over the galaxy, indicating that the stellar population of the most ancient stars differs between fields. We estimate that $\sim$10% of the luminous mass of the Andromeda disk resides in this extended disk component, beyond the 4 scale length cutoff observed in most galaxies. However, this region may account for $\sim$30% of the total angular momentum of the galaxy.

The spatial substructures that form the outer edge of this system are almost certainly no longer gravitationally bound and will disappear as spatially coherent entities within $\sim$200 Myr. However, the existence of these substructures indicates a formation mechanism by mergers and implies that the extended disk is still forming, although we seem to be observing it at the very tail end of its formation period. It is unclear at this point whether the extended disk was formed by multiple accretion events or by a single large event, although the latter possibility appears more plausible given the present data.

Many questions remain to be answered. Is the extended disk a continuation of the thin disk, or is it a separate component? Was the merger, or were the mergers, that formed the extended disk responsible for the formation of the $R^{1/4}$-law halo of Andromeda? Why is the extended disk closely aligned with the thin disk? Why is it not extremely warped?

The surface brightness of this structure, 27–31 mag arcsec^{-2} in its outer regions, places it beyond what would be classified as "disk" in more distant systems. Although such faint surface brightness levels are extremely challenging to observe, by resolving individual stars it will be possible to ascertain whether the extended disk is a particularity of M31 or whether similar components are present in other galaxies. Further work is also needed in the Milky Way to study the distant stellar populations hidden by foreground populations in the Galactic plane, and to understand the nature of the structures recently unveiled at the edge of the Galactic disk and beyond (Newberg et al. 2002; Ibata et al. 2003; Martin et al. 2004a, 2004b; Majewski et al. 2004; Rocha-Pinto et al. 2004, 2005), and their relation to the vast extended disk in the Andromeda galaxy.

R. I. would like to thank Françoise Combes and Bernd Vollmer for very helpful comments and suggestions, Jasonjot Kalirai and Michael Beasley for comments on a draft version of this manuscript, and Greg Wirth for his invaluable and enthusiastic help and support. S. C. C. thanks Luc Simard for helpful discussions and acknowledges support from NASA. G. F. L. acknowledges support through the ARC DP0343508.

REFERENCES

Abadi, M., Navarro, J., Steinmetz, M., & Eke, V. 2003, ApJ, 597, 21
Avila-Reese, V., Firmani, C., & Hernández, X. 2002, in New Quests in Stellar Astrophysics: The Link between Stars and Cosmology, ed. M. Chavez et al. (Dordrecht: Kluwer), 83
Beasley, M., Brodie, J., Strader, J., Forbes, D., Proctor, R., Barmby, P., & Huchra, J. 2004, AJ, 128, 1623
Bellazzini, M., Ibata, R., Monaco, L., Martin, N., Irwin, M., & Lewis, G. 2004, MNRAS, 354, 1263
Binney, J., & Tremaine, S. 1987, Galactic Dynamics (Princeton: Princeton Univ. Press)
Bland-Hawthorn, J., Vlajić, M., Freeman, K., & Draine, B. 2005, ApJ, 629, 239)
Brinks, E., & Burton, W. 1984, A&A, 141, 195
Brown, T., Ferguson, H., Smith, E., Kimble, R., Sweigart, A., Renzini, A., Rich, M., & VandenBerg, D., A. 2003, ApJ, 592, L17
Burstein, D., et al. 2004, ApJ, 614, 158
Carretta, E., & Gratton, R. 1997, A&AS, 121, 95
Chapman, S., Blain, A., Ivison, R., & Smail, I. 2003, Nature, 422, 695
Chiba, M., & Beers, T. 2000, AJ, 119, 2843
Crane, J., Majewski, S., Rocha-Pinto, H., Frinchaboy, P., Skrutski, M. F., & Frinchaboy, P. M. 2003, ApJ, 594, L119
Dalcanton, J., & Bernstein, R. 2002, AJ, 124, 1328
Davis, M., et al. 2003, Proc. SPIE, 4834, 161
Dehnen, W., & Binney, J. 1998, MNRAS, 298, 387
Durrell, P., Harris, W., & Pritchet, C. 2001, AJ, 121, 2557
———. 2004, AJ, 128, 260
Evans, N., Wilkinson, M., Guhathakurta, P., Grebel, E., & Vogt, S. 2000, ApJ, 540, L9
Ferguson, A., Irwin, M., Ibata, R., Lewis, G., & Tanvir, N. 2002, AJ, 124, 1452
Ferguson, A., Johnson, R., Faria, D., Irwin, M., Ibata, R., Johnston, K., Lewis, G., & Tanvir, N. 2005, ApJ, 622, L109
Ferguson, A., Wyse, R., Gallagher, J., & Hunter, D. 1998, ApJ, 506, 19
Fusi Pecci, F., Bellazzini, M., Buzzoni, A., De Simone, E., Federici, L., & Galleti, S. 2005, AJ, 130, 554
Galleti, S., Bellazzini, M., Federici, L., & Fusi Pecci, F. 2005, A&A, 436, 535
Gilmore, G., & Reid, N. 1983, MNRAS, 202, 1025
Greve, T., et al. 2005, MNRAS, 359, 1165
Hammer, F., Flores, H., Elbaz, D., Zheng, X., Liang, Y., & Cesarsky, C. 2005, A&A, 430, 115
Hernquist, L. 1992, ApJ, 400, 460
———. 1993, ApJ, 409, 548
Holland, S., Fahlman, G. G., & Richer, H. B. 1996, AJ, 112, 1035
Hurley-Keller, D., Morrison, H., Harding, P., & Jacoby, G. 2004, ApJ, 616, 804
Huxor, A., Tanvir, N., Irwin, M., Ferguson, A., Ibata, R., Lewis, G., & Bridges, T. 2004, in ASP Conf. Ser. 327, Satellites and Tidal Streams, ed. F. Prada, D. Martinez-Delgado, & T. Mahoney (San Francisco: ASP), 118
Huxor, A. Tanvir, N., Irwin, M., Ibata, R., Collett, J., Ferguson, A., Bridges, T., & Lewis, G. 2005, MNRAS, 360, 1007
Ibata, R., Chapman, S., Ferguson, A., Irwin, M., & Lewis, G. 2004, MNRAS, 351, 117
Ibata, R., Irwin, M., Lewis, G., Ferguson, A., & Tanvir, N. 2001a, Nature, 412, 49
———. 2003, MNRAS, 340, L21
Ibata, R., Lewis, G., Irwin, M., & Cambrésy, L. 2002, MNRAS, 332, 921
Ibata, R., Lewis, G., Irwin, M., Totten, E., & Quinn, T. 2001b, ApJ, 551, 294
Irwin, M., & Trimble, V. 1984, AJ, 89, 83
Katz, N., & Gunn, J. 1991, ApJ, 377, 365
Kennicutt, R. 1989, ApJ, 344, 685
Klypin, A., Kravtsov, A., Valenzuela, O., & Prada, F. 1999, ApJ, 522, 82
Klypin, A., Zhao, H.-S., & Somerville, R. 2002, ApJ, 573, 597
Lauer, T., et al. 1993, AJ, 106, 1436
Loinard, L., Allen, R., & Lequeux, J. 1995, A&A, 301, 68
Martin, N. F., Ibata, R., Bellazzini, M., Irwin, M., Lewis, G., & Dehnen, W. 2004a, MNRAS, 348, 12

Martin, N., Ibata, R., Conn, B., Lewis, G., Bellazzini, M., & Irwin, M. 2004b, MNRAS, 355, L33
Majewski, S., et al. 2004, ApJ, 615, 738
McConnachie, A., Irwin, M., Ibata, R., Lewis, G. Ferguson, A., & Tanvir, N. 2005, MNRAS, 356, 979
McConnachie, A., Irwin, M., Lewis, G., Ibata, R., Chapman, S., Ferguson, A., & Tanvir, N. 2004, MNRAS, 351, L94
Moore, B., Ghigna, S., Governato, F., Lake, G., Quinn, T., Stadel, J., & Tozzi, P. 1999, ApJ, 524, L19
Morrison, H., Harding, P., Perrett, K., & Hurley-Keller, D. 2004, ApJ, 603, 87
Mould, J., Kristian, J., & Da Costa, G. 1984, ApJ, 278, 575
Newberg, H., et al. 2002, ApJ, 569, 245
Peñarrubia, J., Kroupa, P., & Boily, C. 2002, MNRAS, 333, 779
Pohlen, M., Dettmar, R., & Lütticke, R. 2000, A&A, 357, 1
Puzia, T., Perrett, K., & Bridges, T. 2005, A&A, 434, 909
Reitzel, D., & Guhathakurta, P. 2002, AJ, 124, 234
Reitzel, D., Guhathakurta, P., & Rich, M. 2004, AJ, 127, 2133
Robin, A., Reylé, C., Derrière, S., & Picaud, S. 2004, A&A, 416, 157
Rocha-Pinto, H., Majewski, S., Skrutskie, M., Crane, J., & Patterson, R. 2004, ApJ, 615, 732
Rocha-Pinto, H., Majewski, S., Skrutskie, M., & Patterson, R. 2005, preprint (astro-ph/0504122)
Ruphy, S., Robin, A., Epchtein, N., Copet, E., Bertin, E., Fouqué, P., & Guglielmo, F. 1996, A&A, 313, L21
Rutledge, G., Hesser, J., & Stetson, P. 1997, PASP, 109, 883
Schaye, J. 2004, ApJ, 609, 667
Schlegel, D., Finkbeiner, D., & Davis, M. 1998, ApJ, 500, 525
Springel, V., & Hernquist, L. 2005, ApJ, 622, L9
Steinmetz, M., & Müller, E. 1995, MNRAS, 276, 549
Summers, F. 1993, Ph.D. thesis, Univ. California (Berkeley)
Thilker, D., Braun, R., Walterbos, R., Corbelli, E., Lockman, F., Murphy, E., & Maddalena, R. 2004, ApJ, 601, L39
Thilker, D., et al. 2005, ApJ, 619, L79
Tóth, G., & Ostriker, J. 1992, ApJ, 389, 5
van der Kruit, P., & Searle, L. 1981, A&A, 95, 105
Velazquez, H., & White, S. 1999, MNRAS, 304, 254
Walterbos, R., & Kennicutt, R. 1987, A&AS, 69, 311
———. 1988, A&A, 198, 61
Walterbos, R., & Braun, R. 1994, ApJ, 431, 156
Wilkinson, M., Kleyna, J., Evans, N., Gilmore, G., Irwin, M., & Grebel, E. 2004, ApJ, 611, L21
Worthey, G., España, A., MacArthur, L., & Courteau, S. 2005, ApJ, 631, 820
Yoachim, P., & Dalcanton, J. 2005, ApJ, 624, 701
Zucker, D., et al. 2004, ApJ, 612, L117